CREATING NEW PHASE TRANSITIONS AS BRIDGES FOR BROKEN ERGODICITY IN CONFINED COLLOIDAL PRISMS

A Thesis

Presented to the Faculty of the Graduate School

of Cornell University

in Partial Fulfillment of the Requirements for the Degree of

Master of Science

by

Prajwal Bangalore Prakash

August 2018

ABSTRACT

Recent advances in the synthesis and fabrication of faceted sub-micron particles with different shapes have spurred interest in using these particles as building blocks for the assembly of targeted complex structures having enhanced optical properties. Several tunable parameters like particle shape, inter-particle interactions and geometry of the assembly, allow the design of a wide range of morphologies and material properties. In this work, Monte Carlo simulations are used to study the entropy-driven assembly of space-filling convex prism shapes; namely, square and hexagonal prisms under parallel slit-confinement, with either hard or soft-repulsive wall potentials. Phases with diverse structural order arise due to the anisotropy associated with the prismatic particle shape and the restriction of the entropic degrees of freedom of these particles by the wall potentials.

In the hard-wall slit-confinement model, the wall separation were varied to explore the 2D and quasi-2D phase behavior of square and hexagonal prisms. Our simulation results for hexagonal prisms revealed two types of first order phase transitions at the quasi-2D confinement separations: 1) solid-solid transition (6-fold symmetry solid $\rightarrow$ 4-fold symmetry solid) occurring through lattice symmetry breaking, and 2) solid-dense liquid-solid (6-fold symmetry solid $\rightarrow$ no order $\rightarrow$ 4-fold symmetry solid). The predicted dense liquid has a density intermediate between those of the two solid phases and has high translational/orientational disorder and mobility. For square prisms, we observe a solid-polycrystalline-solid phase transition where a lattice spacing rearrangement gives rise to the polycrystalline phase having multiple locally ordered do-

mains.

The unusual phase transitions predicted in this work for the hard confinement model are attributed to the broken ergodicity associated with a dynamically disconnected rotational phase space accessible to the particles. Indeed, for a narrow range of slit separations, particles have two distinct and dynamically disconnected rotational states: *unflipped* (with prism face parallel to wall plane) and *flipped* (with prism side parallel to wall plane), which cast distinct projection areas over the wall plane and lead to different 2D tessellating lattices. As an experimentally viable strategy to dynamically bridge those rotational states but still retain the observed hard-slit phase behavior, a soft-repulsive wall model was also investigated.

BIOGRAPHICAL SKETCH

Prajwal Bangalore Prakash was born in Mysore, India in 1990. After completing his schooling in 2008, he moved to Mangalore for his undergraduate studies. In 2012, he completed his Bachelor's degree in Chemical Engineering from National Institute of Technology Karnataka, Surathkal. He worked as a Research Assistant under Prof. Ganapathy Ayappa at Indian Institute of Science Bangalore and later joined the Chemical Engineering M.Eng. program at Cornell University in 2016. During his M.Eng. program, he joined Prof. Fernando Escobedo's group in the Robert Frederick Smith School of Chemical and Biomolecular Engineering at Cornell University to complete his M.Eng. project and later decided to continue his graduate studies with a Master of Science degree. Under Prof. Fernando Escobedo's guidance, he worked on studying the self-assembly of colloidal prisms in confinement as part of his master's thesis. He will be joining the PhD progam continuing his research with Dr. Escobedo, starting Fall 2018.

ACKNOWLEDGEMENTS

I would like to sincerely thank my thesis advisor Prof. Fernando Escobedo for his constant support and encouragement to pursue further graduate studies at Cornell University. His patience and guidance have helped me throughout my research and writing endeavors. I would like to thank Prof. Abraham Stroock for helping me gain insight into the experimental aspects of my research project, providing me a more holistic perspective. I would also like to thank Prof. Tobias Hanrath for useful discussions and giving me an opportunity to perform some of the related experiments in his lab. I also thank Prof. Itai Cohen, Prof. Chekesha Watson, and Prof. Susan Daniel for allowing access to their experimental equipment and guidance.

I am also grateful to Unmukt Gupta and Dr. Mihir Khadilkar, current and previous graduate students in the Escobedo group, for their excellent mentorship during the initial stages of the project. I would also like to thank Prof. Carlos Avendaño, University of Manchester, for his help with the Floppy Box algorithm. I also thank Dr. Mayank Misra, Yangyang Sun, Mohammed Alshammasi, Abhishek Sharma, Mohammed Alhashim, Jay Gandhi, Meera Ramaswamy, Eric Schwen, Jen-Yu Huang, Rohit Singh, and Han-Yuan Liu for helpful discussions throughout the course of this research project. I would like to acknowledge partial funding support from U.S. National Science Foundation award CBET-1402117.

TABLE OF CONTENTS

LIST OF FIGURES

CHAPTER 1

INTRODUCTION

Assemblies of colloidal particles have promising functional applications as active constituents of photovoltaic devices [1], optical films [2], catalysts [3] and optical sensors [4]. Recent advances in synthesis of faceted sub-micron particles with different shapes has spurred interest in using these particles as basic building blocks for the assembly of targeted complex structures. The type of order and symmetry of these structures can be tuned by controlling such properties as particle geometry [5, 6], interparticle interactions (chemical *patchiness*) [6], depletion forces [7–9], and external fields including hard/soft wall confinement [10–14]. The review article by Min et.al [15] highlights the importance of purely entropic and directed-assembly (involving interparticle and external forces) to obtain targeted colloidal structures.

An active area of research during the last few decades has been the synthesis and assembly of anisotropic colloidal particles to attain Photonic Bandgap (PBG) crystals. The colloidal particle sizes forming the PBG crystals are typically 1 nm − 1 micron and the length scale of the periodic structures formed by these particles is proportional to the wavelength of light in the band gap [16–18]. This unique relationship between the colloidal structure and light wavelength provides the basis for controlling the flow of light through the crystal structure by tuning the colloidal particle shape and material [19–21]. Understanding the assembly mechanism of colloidal particles can allow devising design strategies for not only PBG crystals but also flexible architected metamaterials with a targeted mechanical properties. Reconfigurable metamaterials have found multiple applications, especially in the flexible electronics industry and have led the

way for research on the development of novel three dimensional (3D) flexible materials. For instance, it has been shown that the structures formed by space filling polyhedral colloids can act as good templates to create 3D flexible materials whose mechanical properties can be tuned by forming specific connections between the polygon faces of these colloids [22]. This application illustrates just one productive connection between the self-assembly of structures from particles of different shapes, and the templating of reconfigurable materials.

It is well known that entropic and external forces play a crucial role in the assembly of nanoparticles, and to understand their interplay it is informative to systematically delineate the isolated effects of each driving force. Hard sphere systems provide a suitable theoretical [23] and simulation model to study the inherent effects of entropic forces on the phase behavior of colloidal systems. The bulk 3D system of hard spheres exhibits a transition from isotropic to an ordered *fcc* crystal phase where the ordered structure is stabilized at high pressures by maximizing translational entropy and minimizing the pressure-volume contribution to the free energy of the system. The hard sphere or a similar *'rigid'* spherical core model having a hard-core exclusion potential, is descriptive of simple systems with particles having isotropic shape and a phase transition driven solely by translational degrees of freedom. Hard-core potentials can also be used to gauge the contribution of particle shape on phase behavior. By introducing anisotropy to the particle shape, the orientational degrees of freedom of the particles also become contributors to the total entropy of the system and can hence influence the type of phase transitions and ordered structures that can be formed. Indeed, hard-core anisotropic particles are able to produce a rich collection of self-assembled novel crystal phases but also phases having partial orientational/translational order. These latter phases are termed

as *Mesophases*, where the assembled particles may have only long-ranged translational order (like plastic solid/rotator phases) or only long-ranged orientational order (like Liquid crystals). Numerous simulation [5, 24–29] and experimental [30–33] studies have reported mesophases for different particle shapes during bulk assembly. The presence of an intermediate mesophase between the isotropic and the fully crystalline state can be seen as an intermediate stepping stone that facilitates the transition from disorder to crystalline order, potentially preventing the disordered phase from *'jamming'* at the high densities needed to encounter the crystal phase.

The equilibrium structures attained by colloidal particles in the bulk are substantially altered when the particles are subjected to geometrical confinement such as inside a parallel hard plate/wedge cell [34], or a spherical [35], or a square [36, 37] cavity bounded by a hard wall. The confinement effect is especially important when the dimensions of the environment are such that only a few particle layers can be accommodated along at least one direction. Due to the small wedge angles used in the wedge-cell confinement, different sections along the plates can be approximated by a parallel hard-plate model with different separations. A rich phase behavior has been observed even for a simple hard sphere model confined between two parallel hard plates as the plate separation is varied relative to the diameter of the sphere [38–43]. As the wall separation increases to fit more than one layer, hard sphere colloids assemble into layers with triangular ($n\Delta$) or square ($n\square$) symmetric crystal structures, depending on the commensurability between the plate separation and size of the sphere, where n represents number of layers. At the intermediate plate separation between the stable region of triangular and square symmetric crystal structures, several phases like buckled ($n\mathscr{B}$), rhombic ($n\mathscr{R}$), and prismatic ($n\mathscr{P}$) lattice with trian-

gular or square base are reported [10]. This sequence of simulated phases has been confirmed through experiments [44]. Recently Peng et.al [45] reported on the formation of an intermediate dense liquid phase during the $5\square \rightarrow 4\Delta$ (solid-solid) transition for the colloidal spheres and provided evidence of a two-step nucleation mechanism.

Several computational and experimental investigations have been carried out to explore the phase transitions in 3D and 2D confined model systems with a variety of particle shapes, including members of the truncated cubes family [11], spherical or mushroom caps [13, 34], two-dimensional hard rectangles [46], hard-disks [47], hard rods [36], hard platelets [48], and dimers [14]. The results from these studies have provided a more complete understanding of the combined effect of particle anisotropy, confinement size and geometry [49], charting the changes in phase behavior as the system approaches 2D confinement. A recent simulation study [11] provided a general roadmap comparing the phase behavior under slit confinement of four different shapes of decreasing degrees of asphericity, namely, perfect cubes, truncated cubes, cuboctahedra and truncated octahedra with that of hard spheres. It was found that the tendency to form phases with hexagonal bond-order symmetry similar to hard sphere model and intermediate phases (between n and n+1 layers and also $n\Delta \rightarrow (n+1)\square$) increases as the asphericity of the particle decreases. If the parallel plate confinement is such that anisotropic particles are restricted to occupy a single monolayer in a single orientational state, their phase behavior can be reproduced using an appropriate 2D model system. The phase behavior can drastically change as the confinement separation allows for the increase in rotational and translational freedom of particles along the plate separation axis. However, within a certain range of confinement separation, the disorder-to-order phase

transition resembles those observed in 2D systems.

This work is focused on mapping the thermodynamic phase behavior of two space-filling convex prism shapes; namely, square and hexagonal prisms, under parallel slit-confinement with hard and soft-repulsive walls. By choosing these aspherical shapes, we intend to explore a quasi-2D confinement that could leverage changes in particle orientation to assemble different structures. The main motivation to work with these prismatic shapes was to exploit the fact that they generate two distinct 2D projections over the wall plane; namely a *flipped* and *unflipped* states corresponding to whether the prism side or face is parallel to that plane, respectively. Transitions between these two states can be seen as a mechanism to access structures with different symmetry and/or lattice spacing. In confining these particles, we are imposing a hindrance to the different possible rotational and translational states that the particles can populate during self-assembly, and for carefully chosen dimensions of the confinement and the particles, we can create disconnected regions in the rotational phase space between the *flipped* and *unflipped* states that causes a *non-ergodic* dynamic behavior in the system. Using "unphysical" specialized Monte Carlo (MC) moves in such hard confinement model, we can overcome the dynamic *broken ergodicity* and map out phase transitions that effectively bridge the disconnected regions of phase space. To physically overcome such *broken ergodicity* and hence dynamically (and experimentally) access the same phase behavior probed by the unphysical MC moves, we propose the use of a soft-repulsive wall model, chosen such that those phase space regions forbidden by the hard walls now simply become low-probability regions.

For the shapes under study, the phase behavior mapped is similar to that

of the 2D model at the conditions where a single monolayer is so strongly constrained (by hard or soft walls) that particles can only exist in their unflipped state. The unflipped-state 2D projections of square and hexagonal prisms: namely squares and hexagons exhibit a KTHNY-type [50] continuous fluid-mesophase transition and a continuous mesophase-solid transition [51]. Our simulations predict interesting phase transitions for the quasi-2D like hard confinement separations (once particles in monolayers can access flipped orientations), especially in the dynamically disconnected phase space region. For example, hexagonal prisms undergo a first-order solid-solid and two-stage solid-dense liquid-solid transitions occurring through lattice symmetry breaking; square prisms undergo solid-polycrystalline-solid transition through lattice-space rearrangement. The two solid phases observed at the intermediate and high volume fractions arise from the *unflipped* and *flipped* particle orientations, respectively, casting two different projected areas against the confinement wall which can tessellate the 2D space.

The rest of the thesis is organized as follows. Chapter 2 describes the hard and soft wall confinement models adopted, and the simulation methods and order parameters used to map and characterize the different phases. Chapter 3 summarizes the phase behavior of hexagonal and square prisms with hard and soft wall confinements and Chapter 4 presents the conclusions of our study.

CHAPTER 2

METHODOLOGY

2.1 Model and Method

Simulations of N hard prisms were carried out using the standard Metropolis Monte Carlo algorithm in an isothermal-isobaric (NPT) ensemble. We focus on two types of prisms: hexagonal and square prisms. The scaled confinement separation is $H^* = H/\sigma$, where H is the distance between walls and σ is the minimum distance between the hard walls that allows for the perfect in-plane particle orientation, which for our systems is simply the height of the particle as shown in Fig 2.1. The hexagonal prism (HP) has three characteristic lengths, L, D and σ which are fixed such that, $L = R\sigma$ and $D = 0.866R\sigma$, where R is the aspect ratio of the particle. The maximum projected area, A_{proj} on the confinement plane (Fig 2.1) for HP is $0.649R^2\sigma^2$ and $R\sigma^2$, when the particles are in perfect *unflipped* and *flipped* states, respectively. R for HP is 2 for hard confining walls and 1.82 for soft confining walls. For square prisms (SP), where L= D, we fix the length of L based on the value chosen for HP and R is chosen to restrict bilayer packing. The values chosen for R are 1.82 for hard-wall and 1.67 for soft-wall confinement. The difference in the projected geometry and maximum projected area of the particles at two different states as shown in Fig. 2.1, affects the phase behavior of each shape at intermediate and higher concentrations. In this study, the hard and soft confinement models correspond to a case without (Fig. 2.1(i)) or with (Fig. 2.1(ii)) a soft layer of varying thickness, a^*=a/σ at one of the hard walls. We consider excluded volume interactions, checking for any overlap between particles and also for each particle with the hard walls using

the Gilbert-Johnson-Keerti algorithm [52,53]. The pair potential (U(r_{ij})) between the particles is given as,

$$U(r_{ij}) = \begin{cases} \infty, & \text{if} \quad r_{ij} < r_{ij}^{max} \\ 0, & \text{otherwise,} \end{cases} \tag{2.1}$$

where, r_{ij} is the distance between the particle centers of mass, r_{ij}^{max} is the maximum r_{ij} distance beyond which overlap cannot occur. The hard and soft repulsive potential ($U(r_i)$) between the particle and the hard-wall and a soft-grafted layer is given by,

$$U(r_i) = \begin{cases} \infty, & \text{if} \quad V_{o,hw}(r_i) \neq 0 \\ \beta V_{o,sw}, & \text{if} \quad V_{o,sw}(r_i) \neq 0 \\ 0, & \text{otherwise,} \end{cases} \tag{2.2}$$

where, r_i is the particle center of mass position, $V_{o,hw}$ and $V_{o,sw}$ are the volumes of the particle overlap with the hard walls and soft grafted layer, respectively (Fig. 2.1), β is the modulus parameter (with range: $1 < \beta < 30$). In our model, we also control the thickness of the grafted layer, $a^* = a/\sigma$ as shown in Fig. 2.1 (ii). We adopt a very simple soft repulsive potential model where β controls the hardness of the grafted layer. The particle overlap volume with the soft layer is computed by constructing the 3D simplex [54] using the polyhedral vertices and centroid overlapping with the soft layer.

For the hard confinement model, we simulate a range of H^* values (imposing periodicity in X-Y plane) that accommodates only a single particle layer, thereby restricting our study to understand the 2D and quasi-2D like phase be-

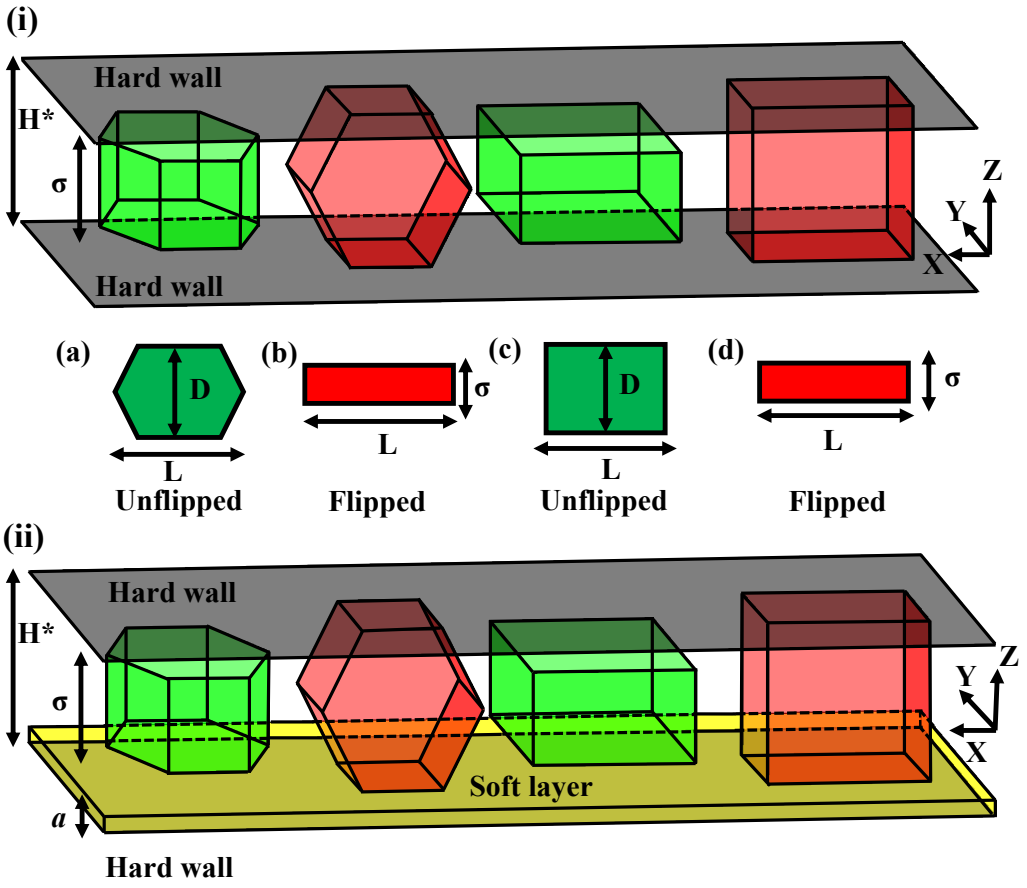

Figure 2.1: Schematic of slit-confinement simulation model, with the plate separation, H^* scaled with respect to the particle height, σ. (i) Confinement model with hard walls. (Middle) The projected geometries of the particle when it assumes *flipped* (out-plane orientation in, red) and *unflipped* (in-plane orientation in green) for hexagonal (a and b) and square (c and d) prisms. (ii) Confinement model with soft layer of thickness, a on the bottom hard wall.

havior. At each H^* value, expansion/compression runs were carried out by equilibrating the system at each pressure step and decreasing/increasing the pressure by small amounts. The expansion and compression runs were carried out to map the phase behavior along the solid and liquid branches and detect any hysteresis present between both runs. For the soft confinement model, we fix the confinement separation, H^* that allows for the dynamic rotation of par-

ticles between the *flipped* (out-plane) and *unflipped* (in-plane) orientation states. We perform compression runs following the same procedure used for the hard confinement model, keeping constant a grafted layer thickness, a^* and modulus parameter, β. The dimensionless pressure, P^*, is given as $P^* = P\sigma^3/k_bT$, where T and k_b are the absolute temperature and Boltzmann constant, respectively. The equation of state was mapped by varying P^* and calculating the packing fraction, $\phi = NV_p/V$, where V_p is the volume of each particles, N is the number of particles and V is the system volume. To minimize finite size effects, we choose the initial system size to have a minimum of 15-20 particles per layer along each of the X and Y dimensions. For compression runs, N = 1254 for hexagonal prisms, and N = 1600 for square prisms; for expansion runs, N = 1352 for hexagonal prisms and N = 1323 for square prisms. For the system with soft layer confinement, N = 1254 hexagonal prisms and N = 1225 for square prisms. At each pressure step, we perform 10^7 Monte Carlo (MC) cycles with the last 3×10^6 cycles used for production runs, where each MC cycle consisted on average of N translational, N rotational, N/10 flip, N/10 two-particle in-plane rotation and 2 volume moves. All move sets implemented obey detailed balance and the step size for the translational, rotational and volume moves are modified based on the fixed acceptance probability value of 0.4, 0.4, and 0.2. We incorporated the *flip* moves that attempt to randomly orient the chosen particle in a plane that is perpendicular to its current orientation. The *flip* move was particularly important to predict the equilibrium structures at different state points for our hard confinement model system having broken dynamic ergodicity, as it helps to access the *flipped* and *unflipped* rotational states that are difficult to sample with standard rotational moves. The two-particle in-plane moves improve ergodic sampling for high-density solid phases and were implemented as fol-

lows. Firstly, two particles are chosen, the first randomly and the second as the particle closest to the first. Next, these candidate particles were rotated in the XY-plane about their combined center of mass (using z-component unit vector) by 90°(clockwise/anticlockwise) [55]. After the move attempt, the acceptance is based on two criteria: (i) the second particle is still the closest to the first one to maintain reversibility, and (ii) no overlap is incurred with the neighboring particles. Each volume move attempt changes the box area and shape in the X-Y dimension (anisotropic moves) during the expansion runs and for compression runs only the box area along the X-Y dimension (keeping a orthogonal box) is allowed to change. Throughout the volume moves (and all other moves) the plate separation remains unchanged.

The initial configuration for the expansion runs is the densest crystal phase at a certain plate separation, H^*. In scenarios where a predictable densest crystal phase cannot be achieved by simple compression runs of larger systems, we adopted the Floppy Box Monte Carlo algorithm [56] to predict the densest crystal phase. Using this algorithm, we simulated systems with a small number of particles (typically N<12) in an isothermal-isobaric (NPT) ensemble, where all moves were accepted or rejected based on the Metropolis criterion, allowing for changes in the box XY-dimensional area and shape during the volume move attempts. Initially, systems with 4, 6, and 8 particles are equilibrated at low pressure for 3×10^6 MC cycles and then subsequently compressed with small pressure steps until reaching a high pressure, $P^* = 8000$. We perform $30 - 50$ such compression runs with different random number seeds and initial configurations, and the final densest crystal phase is determined from its relative occurrence frequency in different compression runs. This structure can be used as the unit cell to construct larger systems, whose stability is further tested by

using NPT simulations with anisotropic volume moves.

The characterization of each phases and transition points in the phase diagram were determined by using various orientational and translational order parameters, mobility calculations, pair correlation, and orientational distribution function.

2.2 Order parameters

2.2.1 Orientational order parameters

Cubatic order parameter

To determine the global orientational order we measure the cubatic order parameter, P_4, which is defined as:

$$\langle P_4 \rangle = \max_{\mathbf{n}} \frac{1}{N} \sum_i P_4(\mathbf{u_i}.\mathbf{n})$$
$$= \max_{\mathbf{n}} \frac{1}{8N} \sum_i (35\cos^4\theta_i(\mathbf{n}) - 30\cos^2\theta_i(\mathbf{n}) + 3) \tag{2.3}$$

where, $\mathbf{u_i}$ is the unit vector along the particle principal axis and $\mathbf{n}$ is the director that maximizes $\langle P_4 \rangle$. The director $\mathbf{n}$ is found using the numerical recipe reported in [57]. This recipe yields three orthogonal directors, $\mathbf{n_1}$, $\mathbf{n_2}$, $\mathbf{n_3}$ and the corresponding values of $\langle P_{41} \rangle$, $\langle P_{42} \rangle$, $\langle P_{43} \rangle$ in decreasing order of magnitude. The three directors are chosen to gauge the in-plane and out-plane alignment of the *flipped* and *unflipped* particle principal axis/faces. Along with the P_4 calculations, we also compute the fraction (F1, F2, F3) of particles principal faces

most aligned with the orthogonal directors to distinguish between the biaxial and nematic (uniaxial) order.

Planar order parameter

The in-plane (*unflipped*) and out-plane (*flipped*) orientations can be discriminated using the planar order parameter $S2$, defined as:

$$\langle S2 \rangle = \frac{1}{N} \sum_i \sin(\mathbf{u_i}.\mathbf{n}) \tag{2.4}$$

where, $\mathbf{u_i}$ is the unit vector along the particle principal axis and $\mathbf{n}$ is the director perpendicular to the wall face. The *flipped* orientation is determined based on the principal orientational unit vector of the particle. Figure. 2.2 (c) shows a simple geometric construction to determine the in-plane (*unflipped*) and out-plane (*flipped*) orientation of each particle in the hard plate confinement model.

The maximum angle, θ between $\mathbf{u_i}$ and $\mathbf{n}$ is obtained when the particle center of mass is fixed at slit central plane and is defined as, $\theta_2 - \cos^{-1}\left(\frac{H^*\sigma}{L_1}\right)$ for *unflipped*, and $\theta_2 + \cos^{-1}\left(\frac{H^*\sigma}{L_1}\right)$ for the *flipped* configuration. This angle can also be computed numerically, by uniformly sampling all orientations for a particle pinned to the central plate separation axis and rejecting configurations that overlap with the hard walls. Based on the result obtained for hard slit walls, we choose 50° to distinguish between *flipped* and *unflipped* configurations (Fig. 2.3). We use the same criterion even for the soft wall confinement model, where the plate separation is large enough to allow for the gradual out-of-plane rotation of the particle.

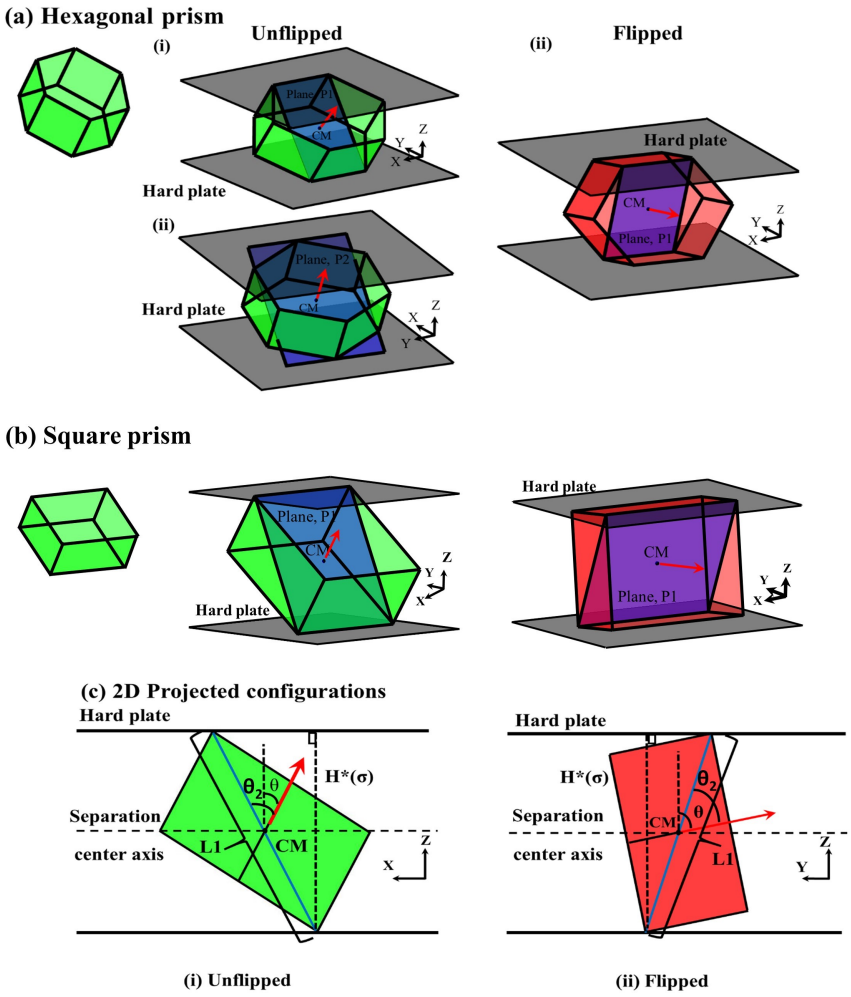

Figure 2.2: Schematic illustrating the *unflipped* (in-plane orientation in green) and *flipped* (out-plane orientation in red) for (a) hexagonal prism and (b) square prism. (c) 2D projection of the *flipped* and *unflipped* configurations where L_1 is the length of the particle diagonal, θ_2 is the angle between the principal vector (red) and particle diagonal (blue), and θ is the angle between the principal particle axis and unit vector perpendicular to the wall plane.

Rotational auto-correlation function

To identify the plastic crystalline behavior of the mesophases observed at higher densities, we use an autocorrelation function that measures the alignment of the

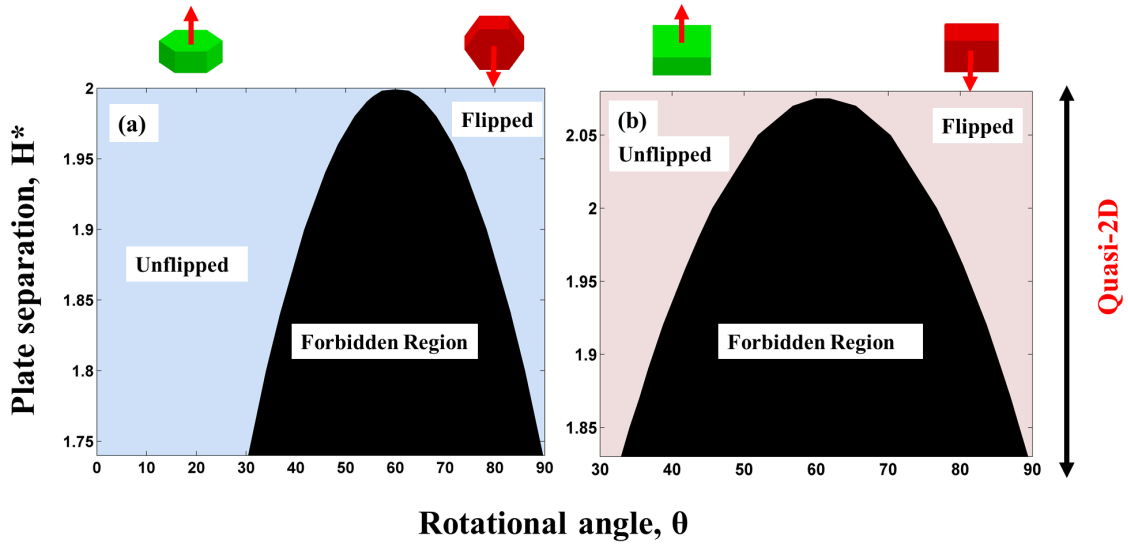

Figure 2.3: Broken continuity in rotational angle phase space with respect to the particle principal axis (red) for (a) hexagonal prism and (b) square prism. The particle center of mass is pinned to the center of the slit to measure the maximum angular difference between the *unflipped* and *flipped* configuration. Forbidden region marks the rotational states inaccessible to the particle.

particle orientation vectors over the MC cycles, and is defined as,

$$\theta_s = \frac{\sum_{i=1}^{N} \sum_{j=0}^{N_{MC}-N_s} \mathbf{u_j^i} \cdot \mathbf{u_{(j+s)}^i}}{N(N_{MC} - N_s)} \tag{2.5}$$

where, $\mathbf{u^i}$ are the particle axes unit vectors, N_s is the number of MC cycles over which the axes alignment is measured, and N_{MC} is the total number of MC cycles. These calculations were performed by using NvT ensemble simulations of equilibrated state points at different densities using "pseudo dynamic" translation and rotation moves. The step size for these pseudo dynamic moves is kept constant and small, corresponding to an average acceptance probability, P_{acc} between 75 and 90 %. The plastic rotator phase can then be characterized by a fast exponential decay of the autocorrelation function indicating that particles are

able to rotate around the particular test axis and over the time scale captured by the exponential decay time constant.

2.2.2 Translational order parameters

Construction of square lattice at high density in hard confinement model

To reveal the inherent square lattice in the columnar/tetratic solid phase at the highest packing density and mark the phase boundary of the tetratic mesophase (at intermediate packing fraction), we follow the construction detailed in (58). The geometric construction of the square lattice from hexagonal and square prisms is depicted in Fig. 2.4. The square lattice constructed for the hexagonal prism system has the dimension σ, since R is defined as $L = 2\sigma$ (Fig. 2.1 b and d). In contrast, a minor mismatch in lattice spacing occurs for the square prism as its aspect ratio is 1.82. The lattice spacing can be determined by the positions of the first and second peaks of the radial distribution function, $g(r)$. For the square lattice constructed for the columnar/tetratic solid phase at the highest packing density, these peak positions are σ and $\sqrt{2}\sigma$ for hexagonal prisms, and σ and 1.1 σ for square prisms. We also constructed a model for a single particle (Fig. 2.4) pinned to the slit center to determine the extra rotational freedom in the XZ plane at quasi-2D confinement separations. This rotations could contribute to defects in lattice spacing, where the maximum particle XZ plane rotation, θ is given by, $\sin^{-1}\left(\frac{H^*\sigma}{2L_2}\right)$ - θ_2. θ_2 and L_2 is 60° and σ for hexagonal prisms and 45° and $\sqrt{2}\sigma$ for square prisms. For hexagonal prisms $0.5° < \theta < 12°$ for $1.74 < H^* < 1.9$, while for square prisms $0.3° < \theta < 3°$ for $1.83 < H^* < 1.91$. These small variations in the XZ plane rotation angles has a minimal effect on the construction of the

ordered lattice for phases at high and intermediate packing fractions.

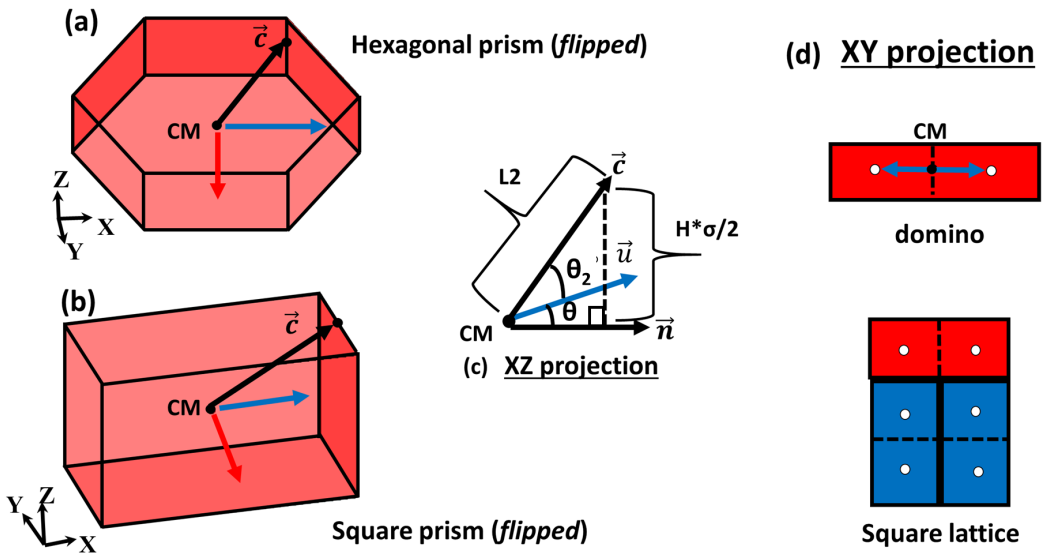

Figure 2.4: Square lattice construction from the *flipped* (a) hexagonal prism and (b) square prism configurations on the XY plane using the particle orientation unit vector (**u**). (c) θ is the maximum angle of *flipped* particle rotation in XZ plane, θ_2 is the angle between vector **c** and **u**, **n** is the global reference unit vector, and L_2 is the magnitude of vector **c**, joining the center of mass and edge midpoint in XZ plane. (d) Domino (rectangular) particle on the XY-plane showing two orientations of the *flipped* particle in *blue* and *red*.

Translational mobility coefficient

To obtain the average accessible local free volume available at different state points, we compute the translational mobility by carrying out NvT ensemble simulations of the equilibrated phases at different densities with a fixed set of translation and rotation moves. We perform the translational moves only in the XY plane and for rotational moves, we sample all three particle orientation axes. The step size for each move set is kept constant such that 75% < P_{acc} < 90% to

mimic *pseudo dynamic* particle motion. To measure the translational mobility coefficient, we calculate the mean square displacement over N_s MC cycles:

$$R_s = \frac{\sum_{i=1}^{N} \sum_{j=0}^{N_{MC}-N_s} |\Delta r^i_{(j+s,j)}|^2}{N(N_{MC} - N_s)} \tag{2.6}$$

where $\Delta r^i_{(j+s,j)}$ is the center of mass displacement of the i^{th} particle between the j^{th} and $(j + s)^{th}$ Monte Carlo (MC) cycles, and N_{MC} is the total number of MC cycles in the simulation. By obtaining the rate of change of the center of mass displacement with MC cycles, we get the mobility coefficient μ_{xy} which quantifies the average in-plane local translational fluctuations for the phases under study.

Bond orientational order parameter

For 2D monolayer structures, the global square (ψ_4) or hexagonal (ψ_6) bond order parameters can be obtained from a complex exponential local n-fold bond orientational order, $\phi_n(\mathbf{r_j})$ for each j particle,

$$\phi_n(\mathbf{r_j}) = \frac{1}{n_j} \sum_{k=1}^{n_j} \exp(in\theta_{jk}) \tag{2.7}$$

where n= 4 or n= 6, θ_{jk} is the angle made by the virtual bond between the particle j and the neighboring particles k with respect to an arbitrary global axis, n_k is the number of nearest neighbors of particle j. The value of n_k is obtained *via*. voronoi tessellation for $n = 6$ and from the four closest neighbors when $n = 4$. The global bond order value is then obtained by calculating an ensemble average of the system,

$$\psi_n = \left\langle \left| \frac{1}{N_r} \sum_{i=1}^{N_r} \phi_n(\mathbf{r_j}) \right| \right\rangle \tag{2.8}$$

All calculations are done by constructing the centroids of the squares for the *flipped* particles as illustrated in Fig. 2.4, where the resulting number of centroids, N_r is (2 N_{flip})+ N_{unflip}.

To further analyze the long or short-range character of the four-fold or six-fold bond order parameter, we compute the bond orientational correlation function given by,

$$g_n(r) = \langle \phi_n(0) \phi_n(\mathbf{r}) \rangle \tag{2.9}$$

where, $g_n(r)$ is the n-fold local bond orientational order at position $\mathbf{r}$.

Structure factor

The translational order is further characterized by analyzing the radial distribution function $g(r)$, and the structure factor $S(\mathbf{k})$, given as [59],

$$S(\mathbf{k}) = \frac{1}{N_r} \left\langle \left[\sum_{i=1}^{N_r} \cos(\mathbf{k}.\mathbf{r_i}) \right]^2 + \left[\sum_{i=1}^{N_r} \sin(\mathbf{k}.\mathbf{r_i}) \right]^2 \right\rangle \tag{2.10}$$

where $\mathbf{k}$ = ($2\pi\ n_x/L_x$, $2\pi\ n_y/L_y$,0) and the values of n_x and n_y are chosen so that the wave vector, $\mathbf{k}$ corresponds to the Bragg peak for the particles position $\mathbf{r_i}$. The resulting number of centroids, N_r is obtained by splitting the XY-projected geometry of the *flipped* particles (Fig. 2.4).

CHAPTER 3

RESULTS AND DISCUSSION

3.1 Phase behavior in hard wall confinement

3.1.1 Hexagonal prisms

The confinement separation, H^* is scaled with respect to the particle height, σ and the values for H^* in the hard and soft confinement model is varied such that the space available only allows the formation of monolayer packing. Figure 3.1 shows the phase behavior by mapping the volume fraction, ϕ, for different phases found at each H^* for hard wall confinement. The phases reported in this study were obtained at different conditions of osmotic pressure, P^*, and plate separation, H^*. In this section, we first describe the quasi-2D like phase behavior in the hard confinement system while in section 3.2 we described the corresponding results from the soft wall confinement model. The 2D phase behavior observed for $H^* < 1.74$ is consistent with that of hard hexagons where the isotropic, hexatic mesophase and hexagonal crystal (1Δ) phases occur with increasing concentration. These results are discussed in Appendix B.1.

Quasi-2D phase behavior

For $0.35 < \phi < 0.48$ and $H^* > 1.85$, the 1Δ solid region is no longer stable and is replaced with a disordered phase, with more particles orienting in the *flipped* state as H^* increases. For $H^* \geq 1.74$ particles can *flip* from an in-plane orientation (*unflipped*) to occupy the space available in the z-axis as it is then wider

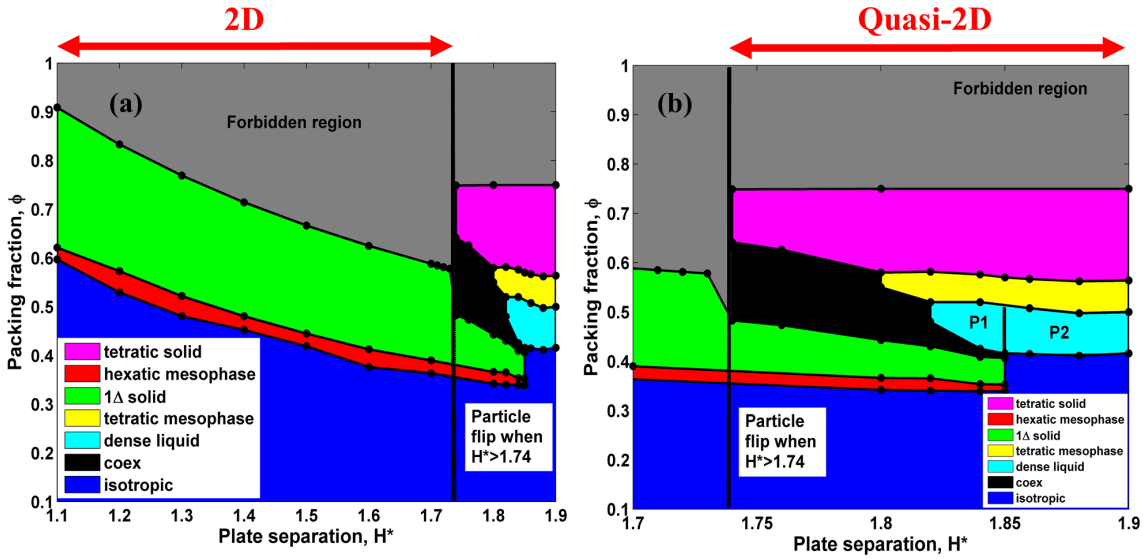

Figure 3.1: Global phase diagram for hexagonal prisms in hard wall confinement ((a) and (b)) at varying confinement separation, H^*. (a) 2D phase behavior for $H^* < 1.74$ and (b) expanded view of quasi-2D phase behavior for $1.74 < H^* < 1.9$.

than the particle dimension, D (Fig. 2.1). Due to the significant particle shape anisotropy, the hexagonal prism cast two very different 2D "shadows" on the XY plane: a smaller area rectangle in the *flipped* state and a larger area hexagon in the *unflipped* state. This footprint duality engenders a unique phase behavior, that combines the packing tendencies of both hexagons and rectangles. We report results from both compression and expansion runs that map the regions where different phases formed at lower and higher packing fractions, respectively. For $1.74 < H^* < 1.85$, an appreciable hysteresis is observed between the compression/expansion runs which can be attributed to a large free energy barrier associated with the transition between the two solid phases, one occurring at intermediate concentration (with six-fold symmetry) and the other at high concentration (with four-order symmetry). Accordingly, we map the higher

density solid branch of the phase diagram with the expansion runs and the intermediate solid and lower density branch with the compression runs.

Tetratic Solid

For $\phi > 0.58$ and $1.74 < H^* < 1.9$, the faces of the *flipped* particles align locally to form the uniaxial and biaxial phases having long range four-fold bond orientational order and square-lattice translational order. These phases can be characterized as being a *tetratic solid*, similar to the phase formed by hard rectangles at high density as described in (58). The tetratic solid regime has two kinds of sub-phase regions (not shown in the global phase map): Mixed (biaxial) and Unmixed (uniaxial) regions, characterized based on the local/long-range alignment of the principal axis of the particles. The cubatic orientational order parameters (P_{41}, P_{42}, and P_{43}) with their corresponding F1, F2, and F3 fractions, and the particle orientation distribution are all used to mark the phase boundary between these two phases. We describe this region of the phase behavior only for $H^* = 1.8$, 1.84, and 1.9, but similar behavior is observed for other H^* values. The fraction of the *flipped* and *unflipped* particles was estimated by using the planar $S2$ order parameter as defined in section 2.2.1. As shown in Fig. 3.2, for $0.58 < \phi < 0.69$ and $H^* = 1.8$, higher values of $0.66 < P_{41} < 0.7$ and $0.63 < P_{42} < 0.67$ are observed compared to $P_{43} \approx 0.37$, indicating the presence of two preferred particle orientations. This behavior is also corroborated by the corresponding values of F1$\approx$ 0.52, F2$\approx$ 0.48, and F3$\approx$ 0. The mixed (biaxial) tetratic solid phase has local orientation of *flipped* (F1 and F2) particles along the two perpendicular in-plane directors forming grain boundaries with different but nearly perpendicular orientations, and the fraction of *unflipped* particles (F3) along the out-plane director

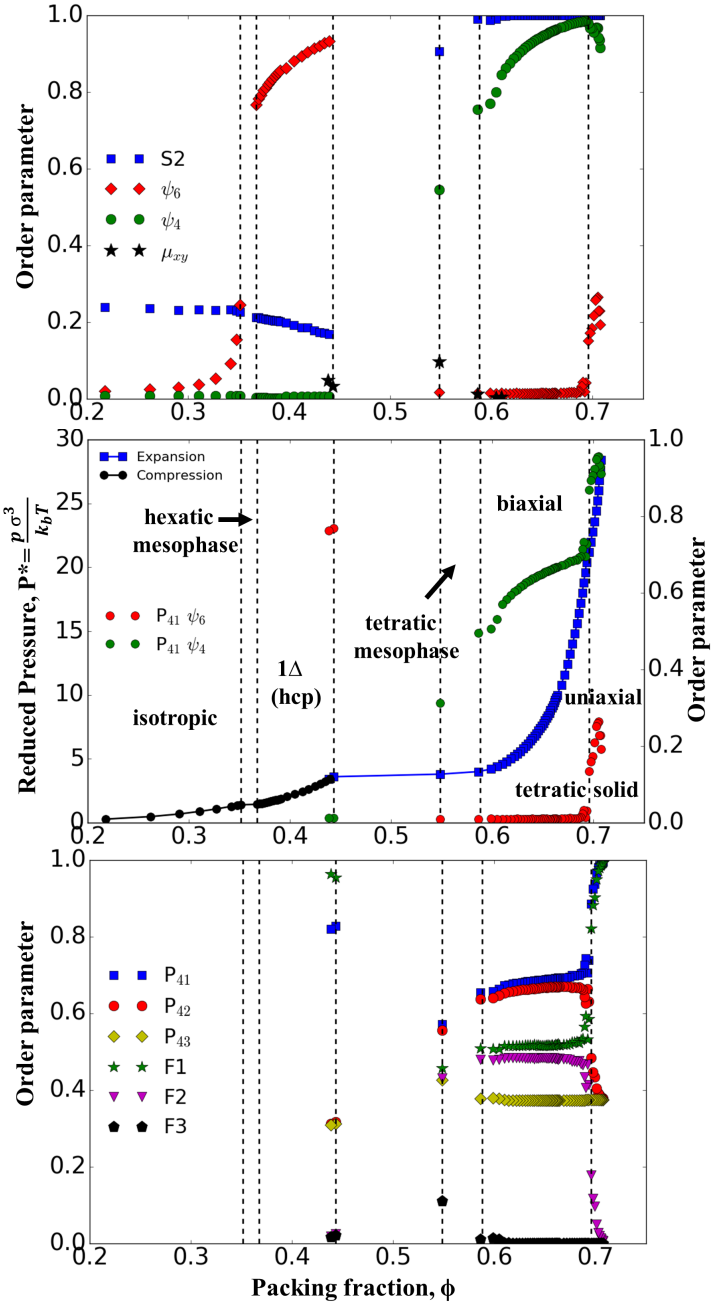

Figure 3.2: Phase behavior of hexagonal prisms under hard plate separation, H^*= 1.8. Dotted lines mark approximate phase boundaries. (Top) Variation of translational mobility coefficient (μ_{xy}), and $S2$, ψ_4 and ψ_6 order parameters with packing fraction, ϕ. (Middle) Equation of state (P^* vs. ϕ) showing compression and expansion runs and cross order parameters $P_{41}\psi_4$ and $P_{41}\psi_6$. (Bottom) Variation of orientational order parameters (P_{41}, P_{42}, P_{43}) and fraction of particles (F1, F2, F3) aligned along the corresponding orthogonal directors.

strongly aligned with z-axis is almost zero (also captured by $S2 \approx 1$).

For the region of the phase diagram showing the transition from the uniaxial to biaxial phase, we observe for $\phi \approx 0.69$ a sharp drop in P_{41}/F1 and a rise in P_{42}/F2, signaling the breaking of the percolation cluster of particles with a particular orientation. A small decrease in the P_{41} and P_{42} upon expansion (decrease in ϕ) in the biaxial region of the phase diagram is expected due to a weaker alignment of the particles in their respective axial directions, while a lower constant value of P_{43}($\approx$0.37) results from the director strongly aligning with the z-axis with all the particles' principal axes pointing perpendicular to it. Figure 3.3 (b) shows a snapshot of the tetratic solid biaxial phase found for $0.76 < \psi_4 < 0.98$ having distinct four-fold peaks in S($\mathbf{k}$) and a four-fold in-plane orientation distribution of the particles' principal axes. The four- and six-fold bond correlation functions, $g_4(r)$ and $g_6(r)$, (Fig. A.1a) show long range tetratic order and short range hexatic order, respectively, and $g(r)$ shows a slow decay of the peak amplitudes, indicative of quasi-long range translational order. These structural characteristics are consistent with the tetratic solid phase observed for hard rectangles. The uniaxial tetratic solid with $\psi_4 \approx 1.0$ exhibits a similar behavior with respect to S($\mathbf{k}$), $g_4(r)$, $g_6(r)$, and $g(r)$ (distinct long-ranged peaks) compared to the biaxial phase, but has a distinct orientational order where all the particle principal axes align in a single direction (Fig. 3.3 (a)). The cross parameter $\psi_4 P_{41}$ reveals a correlation between the principal particle orientation (P_{41}) and the nearest neighbor bond orientational (ψ_4) parameter. For $0.58 < \phi < 0.69$ and $H^* = 1.8$, $\psi_4 P_{41}$ shows a stronger contribution from ψ_4 compared to the small variation in $0.66 < P_{41} < 0.7$, indicative of the formation of local clusters of well-packed particles with similar orientation (Fig. 3.3 (b)). For the $\phi >$ 0.69 region, P_{41} contributes more to the trends in the cross parameter, as the

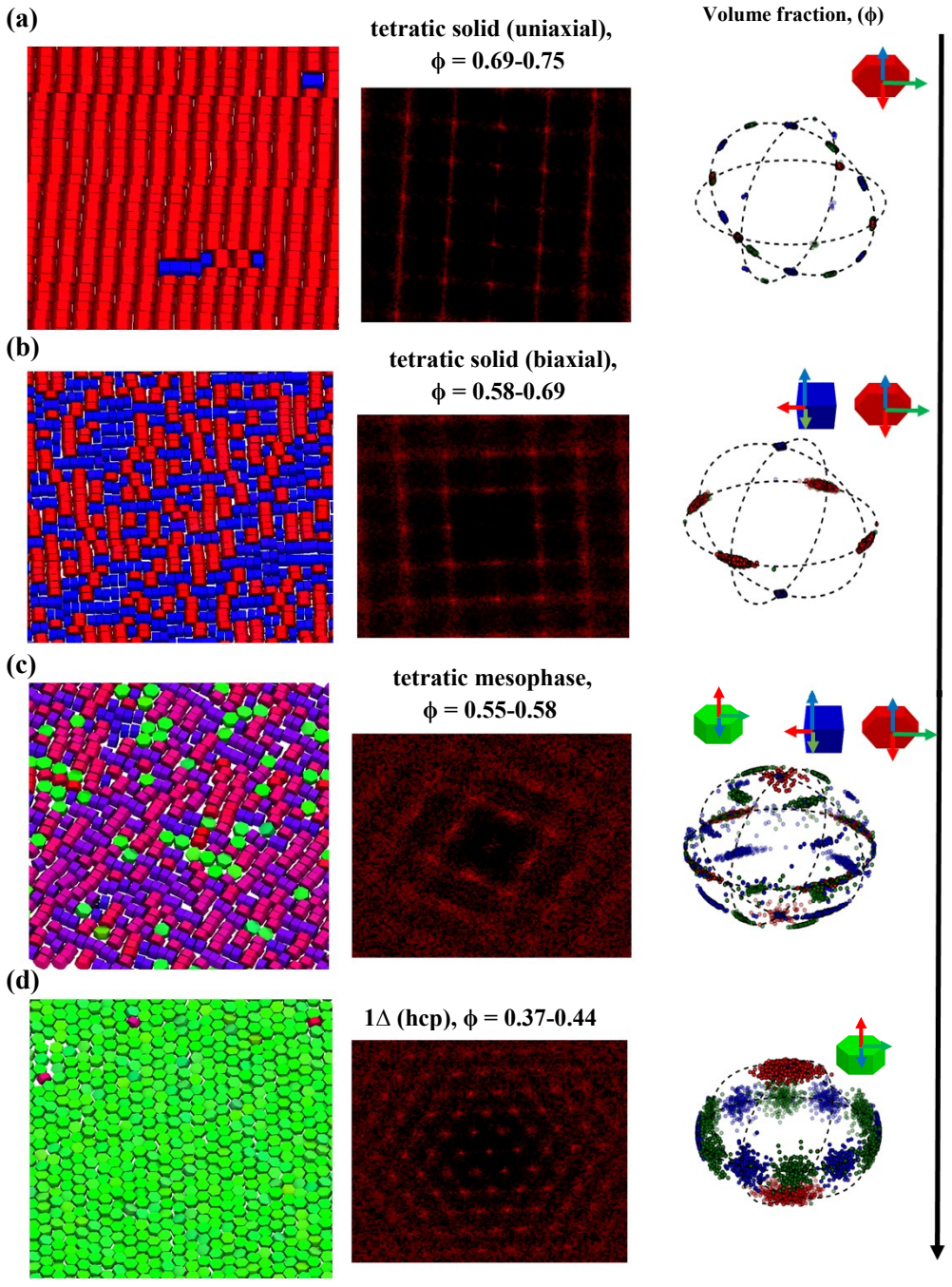

Figure 3.3: Equilibrium structures of hexagonal prisms at different concentrations when the hard plate separation is H^*= 1.8. Representative snapshots, structure factors, and particle orientational distribution functions for stable phases ((a)-(d)) with increasing volume fraction, arranged from bottom to top.

major transformation occurs in the particle orientation. A slight decrease in ψ_4 or increase in ψ_6 (hexagonal order) with ϕ is observed in this region, which is attributed to the sliding/defects between layers, similar to those seen smectic phases [5, 60]. For H^*= 1.84 and $\phi > 0.58$, Fig. 3.5 shows that P_{41} and P_{42} values are greater than 0.6 and F1 = 0.52 and F2 = 0.48, respectively. The behavior of S($\mathbf{k}$), particle orientation distribution (Fig. 3.6) and correlation functions ($g_4(r)$, $g_6(r)$, and $g(r)$) (Fig. A.2) are all consistent with the structural properties of the tetratic solid biaxial phase.

For H^*= 1.9 (Fig. 3.9), the $0.56 < \phi < 0.61$ region is also identified as a tetratic solid with biaxial order (Fig. 3.10), while the $\phi > 0.61$ region as a tetratic solid with uniaxial order. A significant rise in P_{41} and F1 is not observed due to the hysteresis between the structures obtained from expansion and compression runs for H^*= 1.9 at $\phi > 0.61$ (Fig. 3.9). Nevertheless, we still observe the demixing of particle orientations along the compression run, which helps demarking the threshold value $\phi_t \approx 0.625$ during the transition (Fig. 3.4). During the biaxial $\rightarrow$ uniaxial order transition, the local boundaries between grains with different orientations dissolved to form a more orientationally ordered structure (Fig. 3.4 (b)-(d)). We note that the presence of grain boundaries in the biaxial phase contributes to the local free-volume entropy and that the mixed state for $0.58 < \phi < 0.61$ is stabilized by the transition between degenerate particle orientation (sampled by the two-particle MC moves). At higher ϕ, the push for packing efficiency (manifested in $p^*\Delta v$, where Δ= demix $-$ mixed state) drives the system to a more orientationally ordered, lower free-energy state, as shown in Fig. 3.4 (a).

The threshold packing fractions, ϕ_t, for the uniaxial $\rightarrow$ biaxial and uniaxial

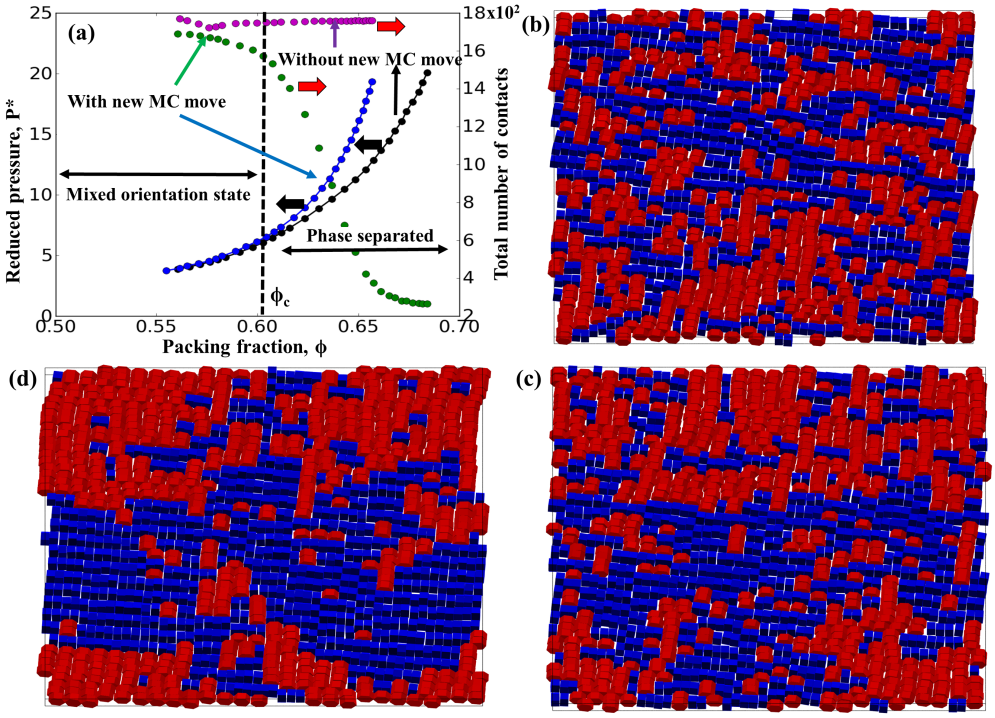

Figure 3.4: Biaxial to uniaxial tetratic solid phases under hard plate separation H^*= 1.9. (a) Comparison of the equation of state (P^* *v.s* ϕ) curves with (black) and without (blue) two-particle in-plane move during compression run. Mixture contacts is the total number of contacts between dissimilar particle orientations (*i.e.*, between red and blue particles). P_c (= 8.08) is the threshold reduced pressure corresponding to ϕ_t (= 0.62). (b)–(d) snapshots showing phase separation during compression runs at (b) P^* = 6.48, ϕ= 0.608, (c) P^* = 8.08, ϕ= 0.623, and (d) P^* = 9.68, ϕ= 0.637

← biaxial phase transition are estimated as 0.69 and 0.62 for the H^*= 1.8 and 1.9, respectively. We did not detect the nematic/smectic phases that are generally observed during a conventional Kosterlitz-Thouless transition for hard rectangles [60], as we only observed long-range translational and four-fold bond-orientational order for the entire region of interest. For H^*= 1.8, ϕ = 0.61 and H^* = 1.84, ϕ = 0.6, the biaxial tetratic solid exhibits a more defined crystalline character as captured by the lower values of mobility coefficient (Fig. 3.2 and

3.5) and the invariance of the autocorrelation function ($\theta_s \approx 1.0$) over the simulation time (with pseudo-dynamic Monte Carlo moves) (Fig. A.6 (b)-(d) and A.7 (b)-(d)).

Tetratic Mesophase

To mark the approximate phase boundaries for the tetratic mesophase, we calculated the correlation functions ($g_4(r)$ and $g(r)$) and S($\mathbf{k}$). The *tetratic* mesophase has (quasi)-long-range tetratic orientation and particle axis orientation order but only short-range translational order. The tetratic order in the system is gauged by the local and global four-fold bond orientation order parameter (ψ_4). As shown in the global phase map (Fig. 3.1), the tetratic mesophase is found for $1.8 < H^* < 1.9$ while for $1.74 < H^* < 1.8$, we only find a stable tetratic solid (biaxial and uniaxial) at the higher concentrations. For H^*= 1.8, 1.84, and 1.9, the tetratic mesophase is found for ϕ ranging between 0.55-0.58, 0.52-0.58, and 0.5-0.56, respectively (Fig. 3.2, 3.5, 3.9). The phase boundary for the tetratic mesophase varies little over the narrow range of H^* values considered. Cubatic order parameters P_{41} and P_{42} decrease and P_{43} increases on expansion for all three confinement separations. The trends in F1, F2, and F3 are similar to those of the cubatic orientational order parameters, showing that the fraction of particles whose principal axes aligned with the in-plane orthogonal directors (*flipped*) decreases and the fraction of particles with the *unflipped* orientation increases during expansion as more local free volume becomes available. This increase in the *unflipped* particle concentration is also captured by the planar order parameter, $S2 < 1$. We observe that the cubatic orientation order parameters are lower than those for the tetratic solid (uniaxial and biaxial) reflecting

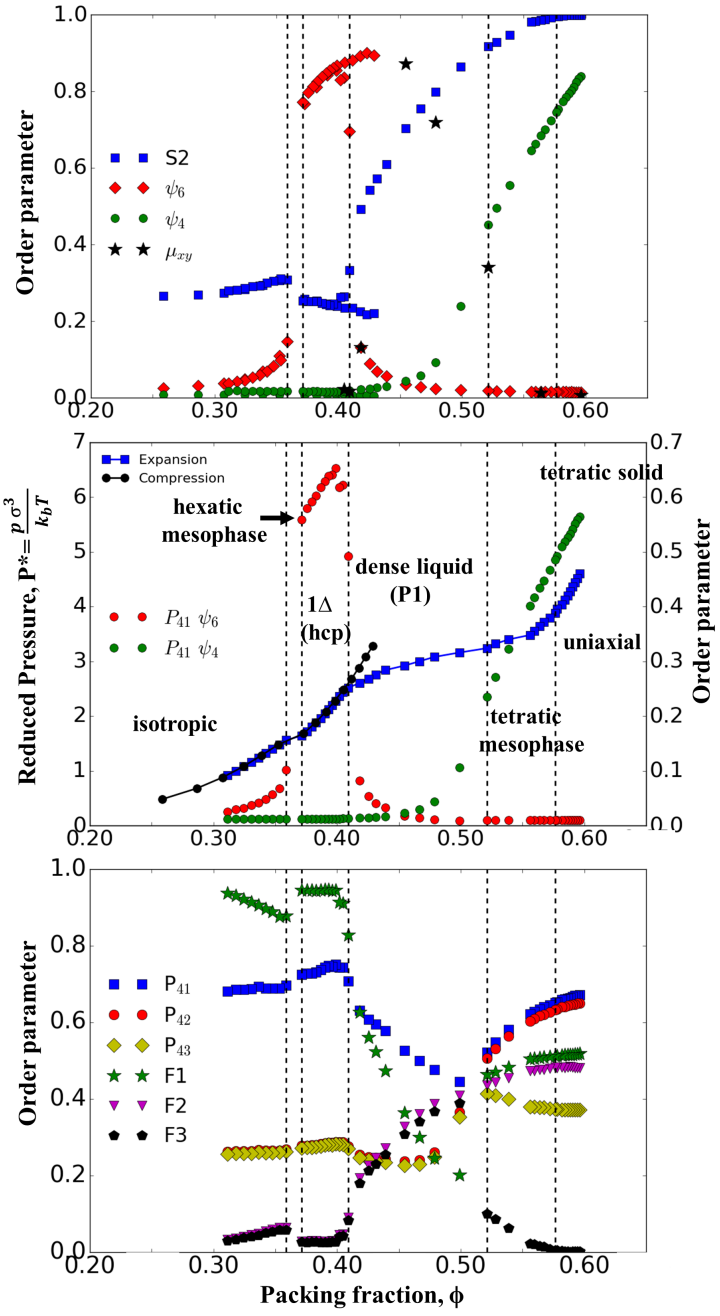

Figure 3.5: Phase behavior of hexagonal prisms under hard plate separation, H^*= 1.84. Dotted lines mark the approximate phase boundaries. (Top) Variation of translational mobility coefficient (μ_{xy}), and $S2$, ψ_4 and ψ_6 order parameters with packing fraction, ϕ. (Middle) Equation of state (P^* *vs.* ϕ) showing compression and expansion runs and cross order parameters $P_{41}\psi_4$ and $P_{41}\psi_6$. (Bottom) Variation of orientational order parameters (P_{41}, P_{42}, P_{43}) and fraction of particles (F1, F2, F3) aligned along the orthogonal directors.

the weaker alignment of the particles' principal faces while maintaining the in-plane four-fold distribution of the particle axes (Fig. 3.3 (c), 3.6 (b), 3.10 (b)). The autocorrelation function for all three particle axes decays linearly with simulation time for the tetratic mesophases observed at ϕ= 0.548 (H^*= 1.8 Fig. A.6 (b)-(d)), 0.56 (H^*= 1.84 Fig. A.7 (b)-(d)), consistent with the trend in the orientational order parameter as the particles have some amount of orientational freedom but still maintain the in-plane four-fold orientation order. The presence of *unflipped* particles (≈ 9-11%) in this region also contributes to the observed decay in the autocorrelation function for the particle axes having in-plane orientation. The weaker alignment of the particles' (*flipped*) principal axis along with the increase in the fraction of *unflipped* particles, also influence the global and local four-fold bond orientational order in the system. Indeed, $0.547 < \psi_4 < 0.77$ for $0.55 < \phi < 0.58$ at H^*= 1.8, $0.45 < \psi_4 < 0.72$ for $0.52 < \phi < 0.58$ at H^* = 1.84, and $0.3 < \psi_4 < 0.79$ for $0.5 < \phi < 0.56$ at H^*= 1.9. In all cases, the corresponding correlation function $g_4(r)$, shown for ϕ= 0.548 (H^*= 1.8), 0.539 (H^*= 1.84), 0.553 (H^*= 1.9), reveals a four-fold order that is stronger among the nearest neighbors and is (quasi)-long ranged (tetratic character), while the $g_6(r)$ function shows a small correlation among the first neighbors and no long-range order (Fig. A.1, A.2, A.3). S(**k**) and $g(r)$ show that the translational order is short ranged at the same conditions, with diffused peaks with four-fold symmetry in S(**k**) and a quick decay of the $g(r)$ peak amplitudes with distance. The translational mobility (μ_{xy}) values calculated for the tetratic regions for H^*= 1.8 and 1.84 (Fig. 3.2, 3.5) are expectedly higher than those for the tetratic solid.

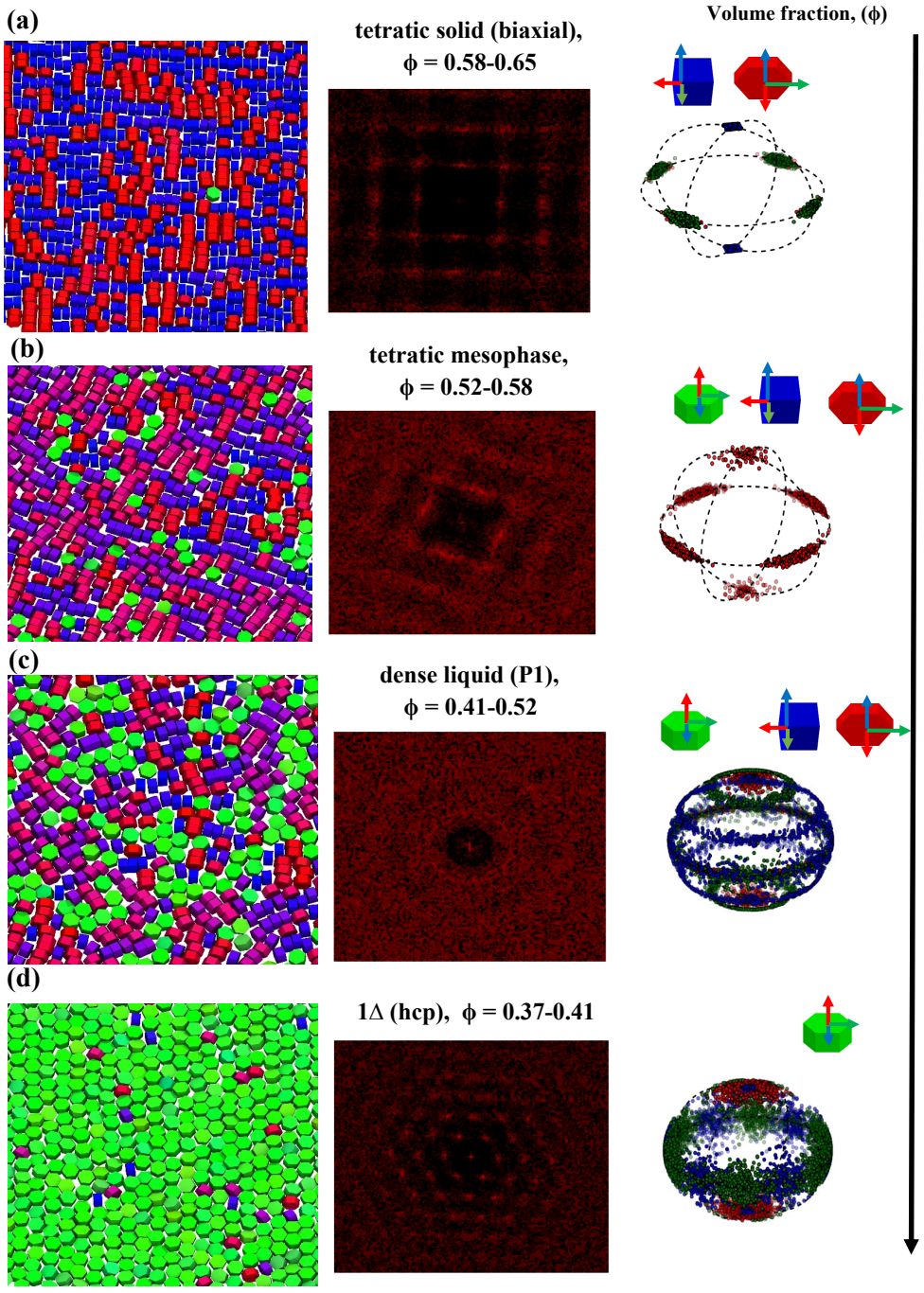

Figure 3.6: Equilibrium structures of hexagonal prisms at different concentrations when the hard plate separation is H^*= 1.84. Representative snapshots, structure factors, and particle orientational distribution functions of stable phases (a)-(d) with increasing volume fraction arranged from bottom to top.

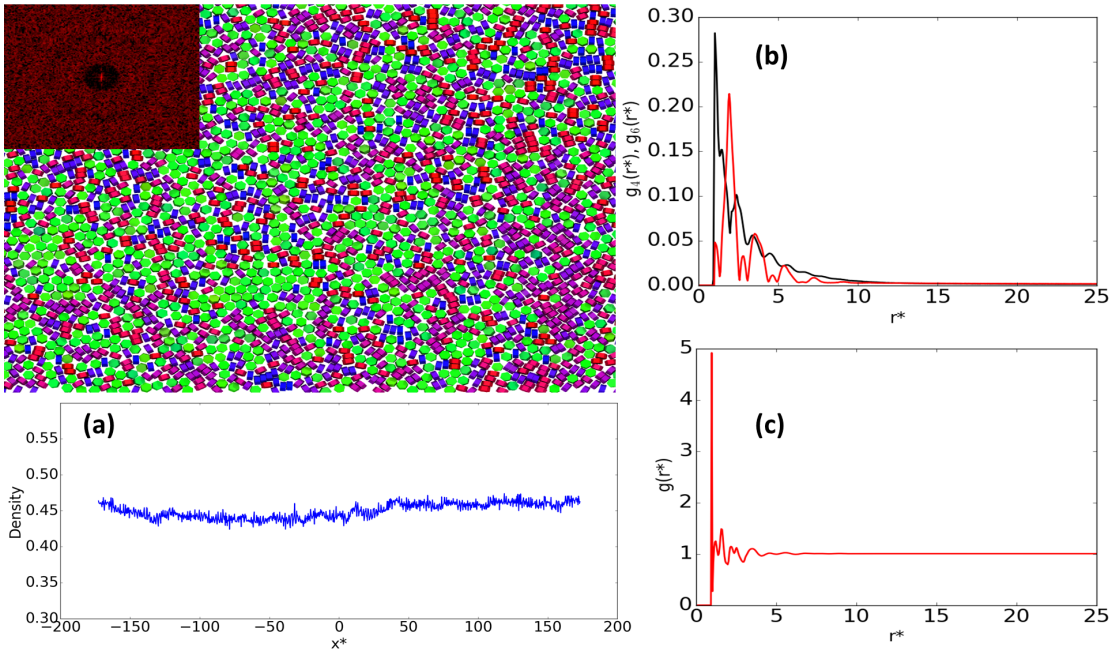

Figure 3.7: Snapshot of the P1 phase obtained for N= 9600 hexagonal prisms from NVT ensemble simulation at ϕ= 0.44 (a), including structure factor as inset. (b) and (c) show various correlation functions.

Solid-Solid and Solid-Liquid-Solid transition

As mentioned before, the 2D phase behavior (hexatic → 1Δ transition) is similar to that of hexagons for $H^* < 1.85$ and $0.35 < \phi < 0.48$, while phases structurally similar to hard rectangles occur at higher concentrations for $1.74 < H^* < 1.9$. We now explore the phase space connecting these two solid phases; namely, the lower density 1Δ and higher density tetratic solid.

For $1.74 < H^* < 1.8$, we observe a first-order solid-solid transition from the tetratic biaxial solid at high densities to the 1Δ solid phase at intermediate densities (ϕ= 0.483-0.44). The two-phase coexistence region on the global phase diagram was obtained from the points where the system transitions from tetratic

solid to 1Δ solid during the expansion runs. For H^*= 1.8, we observe a small region of the tetratic mesophase (0.55 < ϕ < 0.58), before the transition to the 1Δ solid with a coexistence $\phi_{1\Delta}$= 0.44 (Fig 3.2). Figures 3.3 (c) and (d) show the snapshots and the structure factors (S(**k**)) of the tetratic mesophase at ϕ= 0.55 and of the 1Δ solid at ϕ= 0.44, revealing their four-fold and six fold symmetry, respectively. Since the characteristics of the tetratic mesophase structure formed at $\phi_{tetratic}$= 0.55 was already discussed in the previous section, we mainly focus here on characterizing the 1Δ solid formed at $\phi_{1\Delta}$= 0.44. P_{41} (=0.84) is larger than P_{42} and P_{43} (≈ 0.31), resulting from the alignment of all particles' principal axes parallel to the out-of plane director which is strongly aligned with the z-axis (also indicated by the high value of F1 ≈ 0.95). The drop of $S2$ from 0.965 ($\phi_{tetratic}$= 0.55) to 0.12 ($\phi_{1\Delta}$= 0.44), is also an indication that most particles have an *unflipped* orientation. The 1Δ solid at ϕ= 0.44 has ψ_6 ≈ 0.95 (ψ_4 ≈ 0) and a higher value of ψ_6 (0.77-0.95) for 0.37 < ϕ < 0.44. Figure A.1 for ϕ = 0.44 and H^*= 1.8 shows that the 1Δ solid exhibits long-range hexatic order ($g_6(r)$) and short-range tetratic ($g_4(r)$) order, while $g(r)$ has pronounced peaks persisting over long distances, indicative of solid-like behavior. Interestingly, the rotational autocorrelation function for the particle axes in the 1Δ solid reveals an exponential decay with simulation time, indicating a rotator/plastic solid character. For the conditions at which the tetratic solid → 1Δ solid transition occur during expansion with 1.74 < H^* < 1.8, the lower density 1Δ solid phase must be stabilized by gains in translational entropy from motions along the z-axis (as μ_{xy} is low) and in orientational entropy from the allowed in-plane particle rotations. In contrast, the high density tetratic solid with their tightly packed *flipped* particles has lower entropy compared to the 1Δ solid due to the small contributions from the in-plane (μ_{xy}) and out-of-plane translational degrees of freedom, and nearly

frozen orientational degrees of freedom. Figure 3.8 (a) shows the increase in the spread of the z-particle distribution functions during the expansion runs as the system undergoes tetratic solid → tetratic mesophase → 1Δ phase transitions for H^*= 1.8.

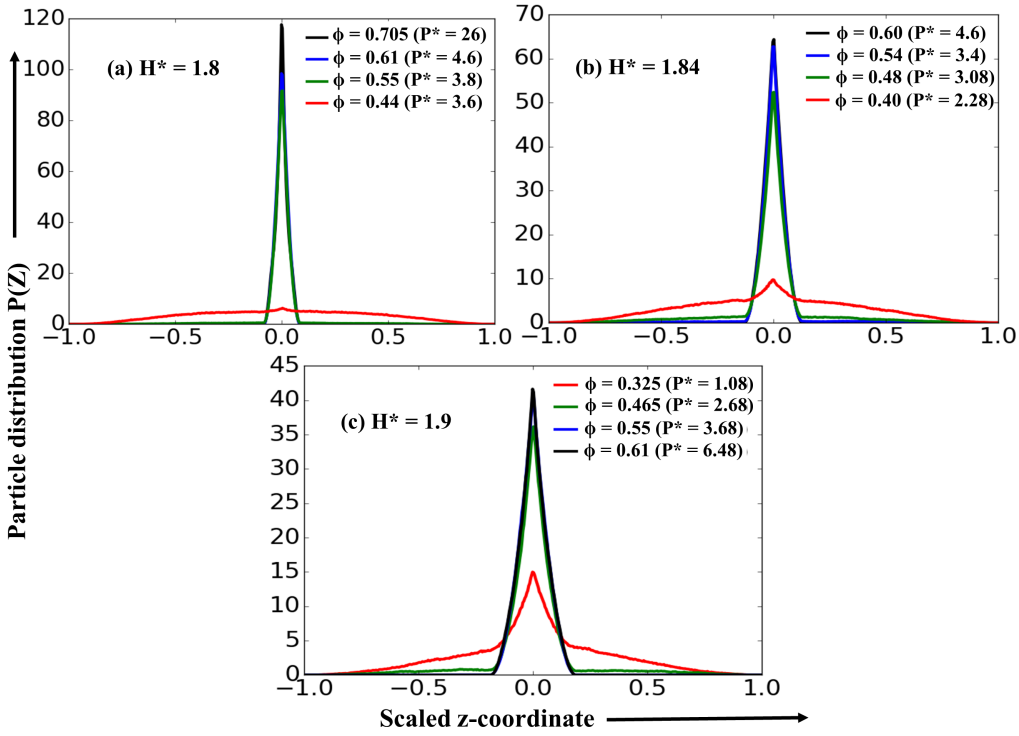

Figure 3.8: Z-coordinate distribution function for hexagonal prisms under different hard plate separation (a) H^*= 1.8 for the tetratic solid uniaxial and biaxial, tetratic mesophase, and 1Δ (hexagonal close packed) solid, (b) H^*= 1.84 for the tetratic solid biaxial, tetratic mesophase, dense liquid (P1), and 1Δ and (c) H^*= 1.9 for the tetratic solid, tetratic mesophase, dense liquid (P2) and isotropic phases.

For H^*= 1.84, we report a second type of phase transition for 0.42 < ϕ < 0.52, where a stable disordered phase, henceforth referred to as "dense liquid" (P1) exists between the tetratic mesophase (ϕ > 0.52) and the 1Δ solid (ϕ < 0.42). Note first that for ϕ > 0.42, a wider tetratic mesophase region is observed compared to the H^*= 1.8 case due to the additional freedom for translation along

the z-axis for the *flipped* particles (resulting in a wider z-particle distribution (Fig. 3.8 b)). The fraction of the *flipped* particles reduces during expansion of the tetratic mesophase as the system is able to gain additional translational and orientational entropy by transitioning to the *unflipped* orientation. These *flipped* → *unflipped* transitions eventually lead to the P1 dense liquid phase for $0.42 < \phi < 0.52$ which lack any structural signature of typical mesophases or solids. Figures 3.6 (c) shows a snapshot, S(**k**), and the orientation distribution of the P1 phase at ϕ= 0.48, which clearly indicates a lack of orientational and translational order (contrast this to the 1Δ solid at ϕ= 0.4 which reveals a six-fold lattice symmetry (Fig. 3.6 d)). The particle axes orientation distribution does show in-plane orientational disorder (of *flipped-unflipped* states) albeit with some discreteness (clustering) due to the rotational symmetry of the hexagonal facets. Upon expansion to $\phi < 0.52$, P_{41} and F1 trends show an inflection at $\phi \approx 0.5$ where their value increases with decreasing ϕ as more particles achieve the in-plane (*unflipped*) orientation. The decrease in P_{42} (F2) and P_{43} (F3) with expansion are due to the increase in in-plane orientation disorder and the fraction of *unflipped* particles. Figure A.7 (b)-(d) shows a quick decay of the rotational autocorrelation function of the three particle axes at two different state points (ϕ = 0.48 and 0.44) of the dense liquid P1 phase. Figures 3.5 and A.2 show that this P1 phase exhibits low translational/orientational order in ψ_4 and ψ_6, $\psi_6 P_{41}$ and $\psi_4 P_{41}$, short-range orientational order in g_4 and g_6, and short-range translational order in $g(r)$. An appreciable increase in the translational mobility is observed as the concentration of the *flipped* particles decreased from 77% at ϕ = 0.48 to 62% at ϕ = 0.44, suggestive of liquid-like behavior. In fact, by forming stable contacts between the *flipped* and *unflipped* particle orientations, more local free volume is created in the P1 phase that allows all particles to rearrange dynamically. On

further expanding the system ($\phi < 0.44$), the translational mobility decreases as the fraction of *unflipped* particles increases forming local solid-like clusters having six-fold bond orientation (high ψ_6) that eventually nucleate the 1Δ rotator solid at ϕ= 0.42. The P1 structure formed at ϕ= 0.44 and 0.48 have clusters of *flipped* and *unflipped* particles having weak tetratic and hexagonal packing order, oriented in random directions (as shown in the orientational distribution plot in Figure. 3.6 (c)).

To rule out the possibility that P1 is a two-phase mixed state (i.e., it lies within a two phase coexistence region) like a metastable tetratic mesophase with incomplete melting of solid clusters, we performed an NVT ensemble simulation at ϕ= 0.44 and 0.48 with N = 9600 particles using an initial well-separated two-phase configuration within an elongated box. One phase was the high-density tetratic biaxial solid phase (at ϕ= 0.6) obtained from the NPT ensemble simulation, while the other phase was an isotropic state chosen from the low density branch of the equation of state such that the overall density of the system studied was either ϕ= 0.44 or 0.48 (where P1 is observed). Figure 3.7 shows the snapshot and the correlation functions ($g_4(r)$, $g_6(r)$, and $g(r)$) at ϕ= 0.44. We found that regardless of the initial conditions the interface between the two phases vanished and the system ended up forming the same P1 phase observed before.

Figures 3.10 (c) and (d) show snapshots for H^*= 1.9 with the dense-liquid phase P2 ($0.42 < \phi < 0.5$) and the isotropic phase ($0.32 < \phi < 0.42$). The S($\mathbf{k}$) features of this P2 phase are very similar to those of the P1 phase obtained for H^*= 1.84 having a mixture of *unflipped* and *flipped* oriented particles. However, the dense-liquid phase P2 transitions directly into the isotropic phase upon expan-

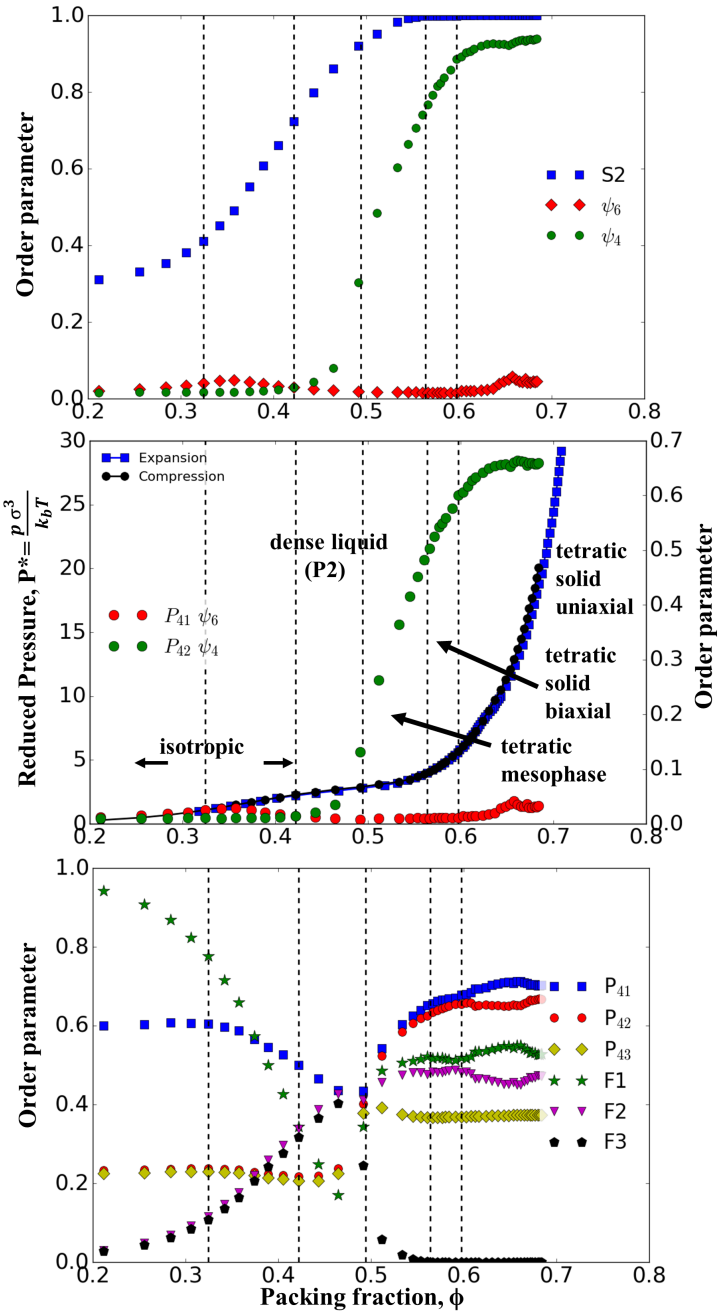

Figure 3.9: Phase behavior of hexagonal prisms under hard plate separation, H^*= 1.9. Dotted lines mark the phase boundaries. (Top) Variation of translational mobility coefficient (μ_{xy}), and $S2$, ψ_4 and ψ_6 order parameters with packing fraction, ϕ. (Middle) Equation of state (P^* *vs.* ϕ) showing compression and expansion runs and cross order parameters $P_{41}\psi_4$ and $P_{41}\psi_6$. (Bottom) Variation of orientational order parameters (P_{41}, P_{42}, P_{43}) and fraction of particles (F1, F2, F3) aligned along the orthogonal directors.

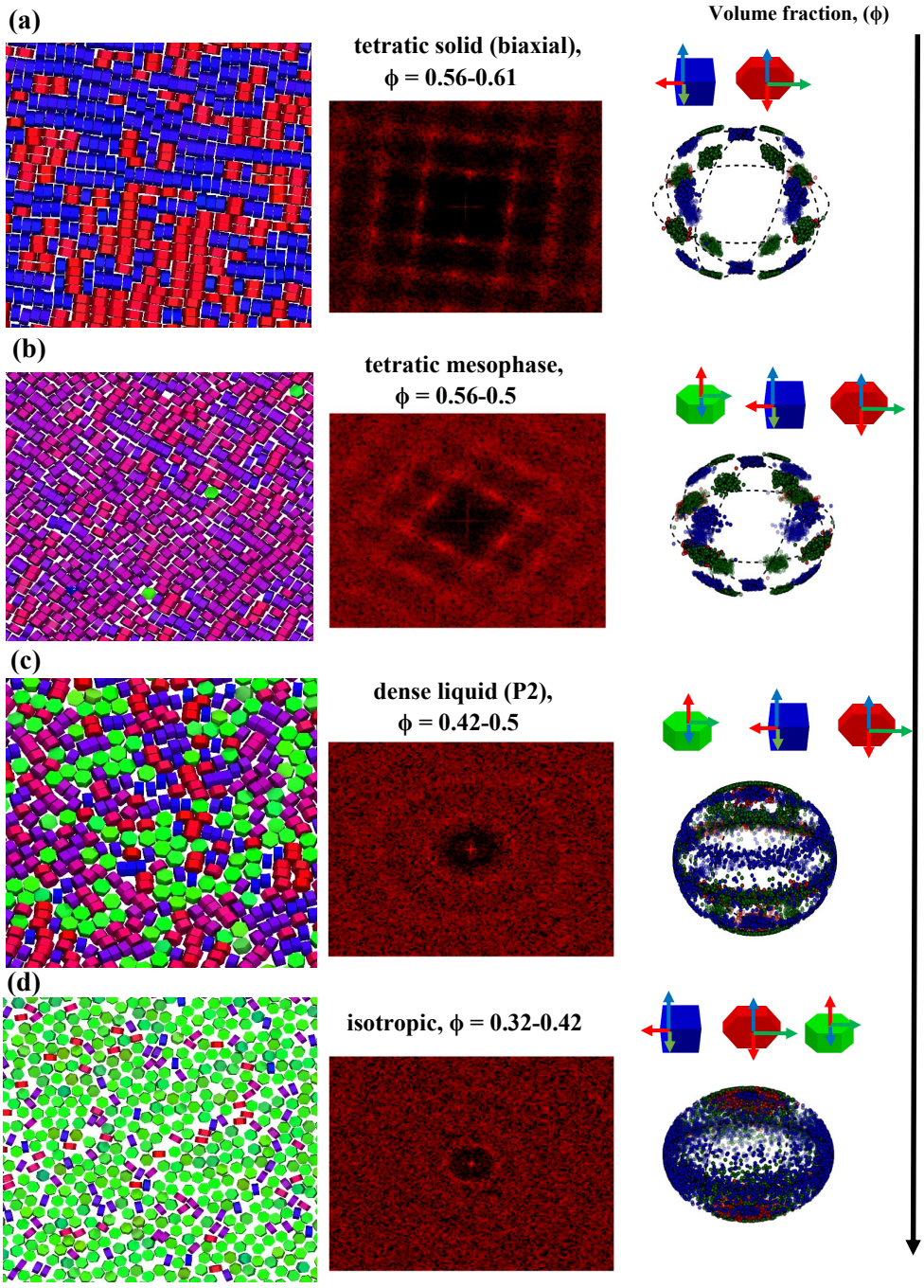

Figure 3.10: Equilibrium structures of hexagonal prisms at different concentrations when the hard plate separation is H^*= 1.9. Representative snapshots, structure factors, and particle orientational distribution functions of stable phases (a)-(d) with increasing volume fraction arranged from bottom to top.

sion without crossing the stable 1Δ solid phase region. The transition between the P2 and isotropic phases can be obtained by both compression and expansion runs as shown in the Fig. 3.9. In the isotropic phase most of the particles have in-plane (*unflipped*) disorder (random orientations) as shown in the orientation particle axes distribution plots (Fig. 3.10 (d)) and by the low values of $S2$ (0.3-0.4) and P_{41} (indicative of out-of-plane alignment of most particles' principal axes). As the isotropic system is compressed to $\phi > 0.32$, more particles start to *flip* as can be seen by the increase in $S2$ and the narrowing of the z-particle distribution (Fig. 3.8 (c)), while no significant four-fold or six-fold bond orientational order develops. Further compressing the system leads to the formation of the P2 phase ($0.42 < \phi < 0.49$) having short range four-fold and six-fold correlation along with no large distance peaks in the radial distribution function $g(r)$ and low values of the cross correlation parameters, $P_{41}\psi_6$ and $P_{41}\psi_4$ (Fig. A.3 and Fig. 3.9).

3.1.2 Square prisms

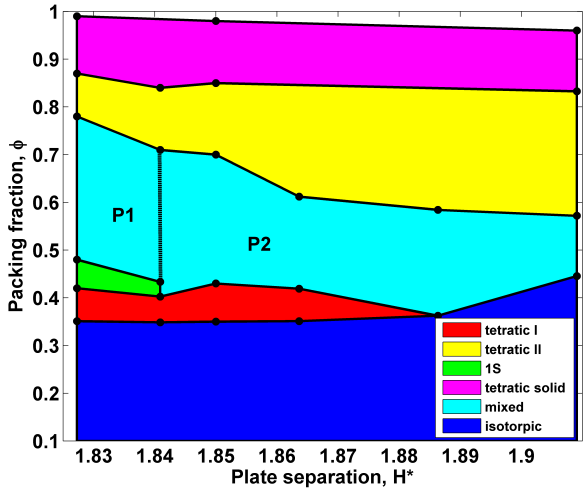

Figure 3.11: Global phase map for the square prism shape particles with hard wall confinement model at varying confinement separation, H^* showing the quasi-2D phase behavior for the confinement separation, H^* 1.83-1.91.

Figure 3.11 shows the phase diagram for hard square prisms showing the phases found at different confinement separations H^* from compression and expansion runs for hard wall confinement. Here we focus on the quasi-2D phase behavior, and defer the better-known 2D phase behavior to the Appendix B.2. For $1.83 < H^* < 1.91$, we find a small hysteresis between the results from expansion and compression runs, even across the transition between two solids. This small hysteresis is likely related to the common four-fold symmetry in the two solid phases so that their phase transition only involves a change in lattice spacing.

Quasi-2D phase behavior

For 1.84 < H^* < 1.89, the 1S solid region observed for H^*=1.83-1.84 is not stable and is replaced by the tetratic-I phase. In such a phase, more particles orient in the *flipped* state (Fig. 3.11) to occupy the free volume available in the z-dimension (noting that L/σ= 1.82 < H^*; see Fig. 2.1). During the transition from the *unflipped* to the *flipped* states, the square prism casts two different "shadows" onto the XY-plane: a larger-area square and a smaller-area rectangle. It is this feature of the particle shape anisotropy that leads to two kinds of 2D packing behavior for a certain range of H^*; namely hard square and hard rectangle tilings.

For higher P^* (corresponding to ϕ > 0.82) and 1.83 < H^* < 1.91, the *flipped* particle faces align locally to form a biaxial tetratic solid (having short-range orientational alignment) but still maintaining long-range four-fold bond orientational and translational order (inherent to the square lattice). This phase behavior is similar to that of the hexagonal prisms at higher density as both square and hexagonal prisms have identical projected geometry (albeit different projected area) when the particles are *flipped*. Figures 3.13 and 3.15 (a) show a snapshot, $S(\mathbf{k})$ and the particle orientation distribution plot for H^*= 1.83 and 1.85, respectively. These show that the tetratic solid has translational order (i.e., four-fold distinct peaks in $S(\mathbf{k})$) and biaxial orientational order (i.e., a four-fold in-plane particle principal axis orientation distribution). For H^*= 1.83 and 1.85 and ϕ > 0.85, P_{41} and P_{42} have higher values compared P_{43} indicating the presence of two preferred particle orientations, a trend also corroborated by the values of F1≈ 0.51, F2≈ 0.49, and F3≈ 0. The mixed (biaxial) tetratic solid phase has local orientation of *flipped* (F1 and F2) particles along the two perpendicular in-plane

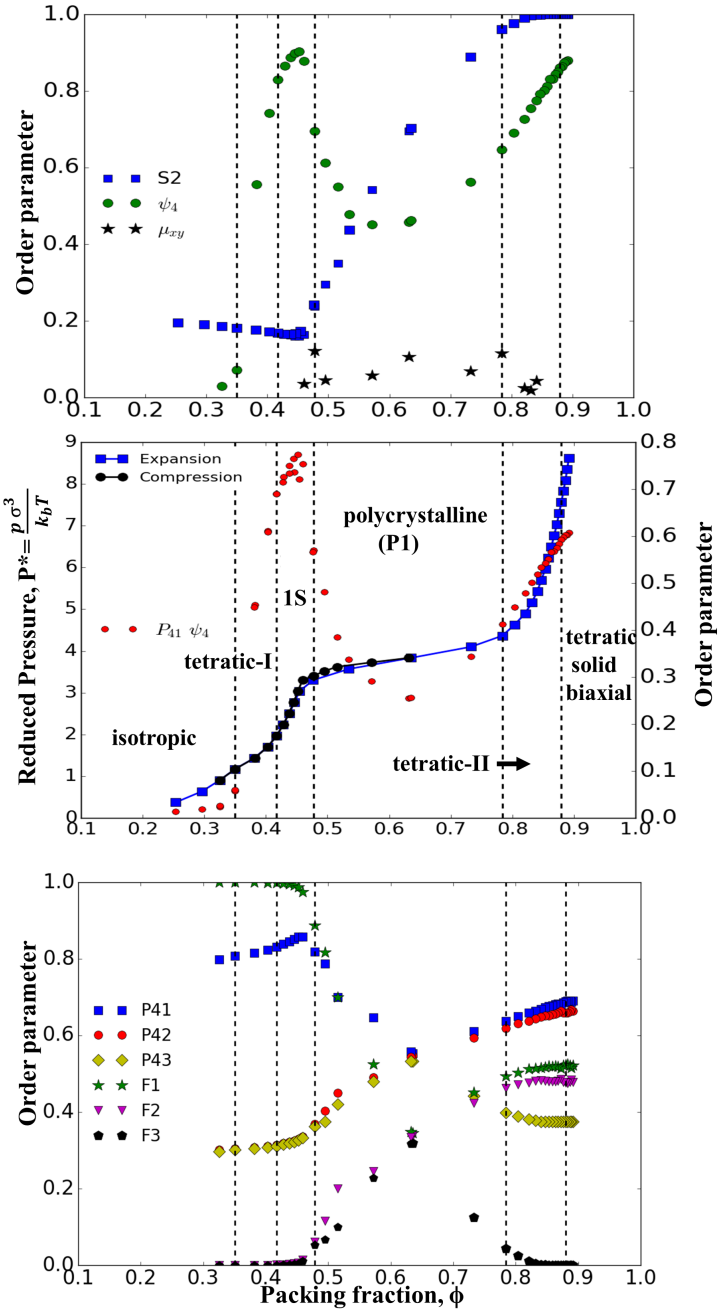

Figure 3.12: Phase behavior of square prisms under hard plate separation, H^*= 1.83. Dotted lines mark the approximate phase boundaries. (Top) Variation of translational mobility coefficient (μ_{xy}), and $S2$, ψ_4 and ψ_6 order parameters with packing fraction, ϕ. (Middle) Equation of state (P^* *vs.* ϕ) showing compression and expansion runs and cross order parameters $P_{41}\psi_4$ and $P_{41}\psi_6$. (Bottom) Variation of orientational order parameters (P_{41}, P_{42}, P_{43}) and fraction of particles (F1, F2, F3) aligned along the orthogonal directors.

directors forming local grains with different orientations while the fraction of *unflipped* particles (F3) along the out-plane director is zero (consistent with $S2 \approx 1$). Further, ψ_4 exhibits high values (> 0.8), $g_4(r)$ shows long-range order and $g(r)$ shows distinct peaks over long distances. Figure A.4 shows the correlation functions for the tetratic solid phase at P*= 8.62 and ϕ= 0.89 for H^*= 1.83 and P*= 7.45 and ϕ= 0.862 for H^*= 1.85. We are unable to pinpoint the phase boundary between biaxial to uniaxial tetratic solids, but the densest crystal phase obtained from floppy box simulations has uniaxial ordering.

An approximate boundary for the tetratic-II mesophase was marked using a combination of features from global (ψ_4, $P_{41}\psi_4$) and local ($g_4(r)$, S($\mathbf{k}$)) order parameters. The structure of the tetratic-II phase is similar to that of the tetratic-I phase found at lower concentrations, but has a different lattice spacing as most of the particles are *flipped* and hence pack more similarly to hard rectangles. The values of $S2$ were $\approx$ 0.2 for the tetratic-I and $\approx$ 0.95-1 for the tetratic-II at both H^*= 1.83 and 1.85, indicating higher fraction of *flipped* orientation particles in the latter phase. Figures A.4 and A.5 show the $g(r)$ for H^*= 1.83 and 1.85 for the tetratic-I and tetratic-II mesophases, evidencing the change in lattice spacing as a reduction in position of the nearest- neighbor $g(r)$ peak from tetratic-I to tetratic-II. For H^*= 1.83 and 1.85 cases discussed in detail, the tetratic mesophases are found for 0.78< ϕ <0.87 and 0.7 < ϕ < 0.85, respectively (Fig. 3.12, 3.16). Examining the cubatic orientational order, we find that on compression P_{41} and P_{42} increases and P_{43} decreases, with similar trends for the corresponding F1, F2, and F3 fractions, indicating an increase in the population of *flipped* particles and stronger alignment of the particles principal faces. Figures 3.13 and 3.15 (b) show snapshots and the in-plane four-fold distribution of the particles axes for H^* 1.83 and 1.85, respectively. They also evidence short-range

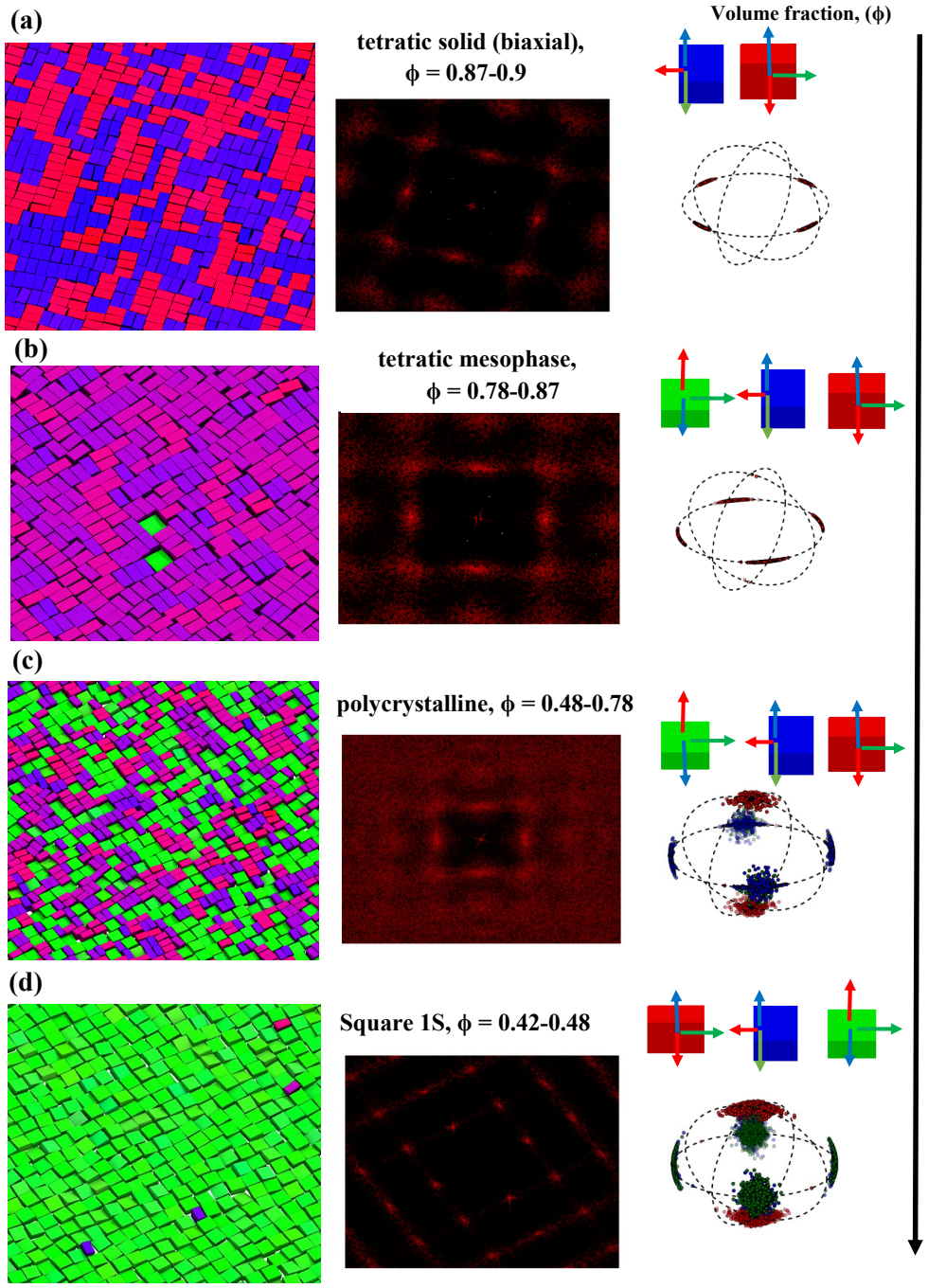

Figure 3.13: Equilibrium structures of square prisms at different concentrations when the hard plate separation is H^*= 1.83. Representative snapshots, structure factors, and particle orientational distribution functions of stable phases (a)-(d) with increasing volume fraction arranged from bottom to top.

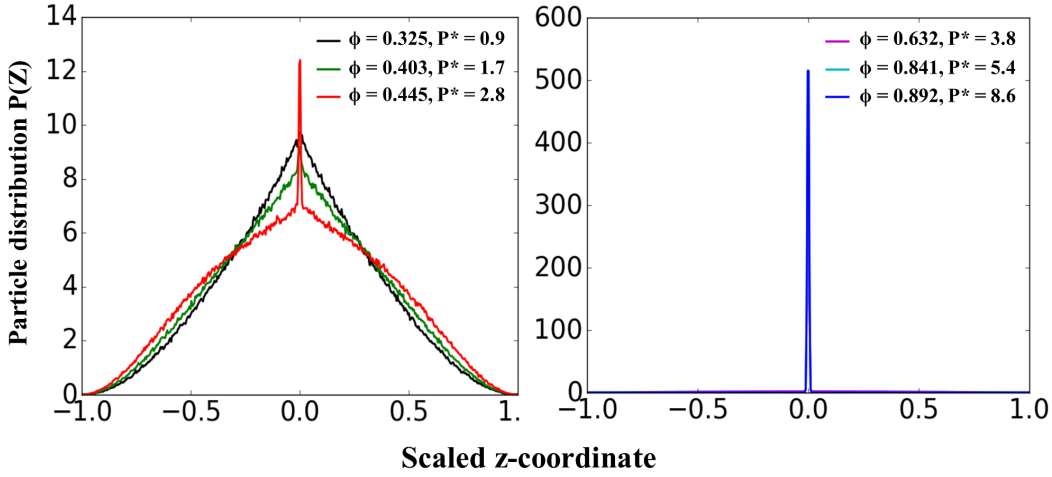

Figure 3.14: Z-coordinate distribution function for square prisms under hard plate separation H^*= 1.83 for the (a) isotropic, tetratic-I, and 1S phases, (b) polycrystalline (P1), tetratic-II and tetratic solid biaxial phases.

translational order by the four-fold diffused peaks in S(**k**) and moderate four-fold bond orientational order with ψ_4 = 0.6-0.82. The results for $g_4(r)$ and $g(r)$ in Fig.A.4 and A.5 reveal that the four-fold order is strongest among nearest neighbors and has (quasi)-long range tetratic character with an average local value of 0.6, while $g(r)$ shows short range order (i.e., peaks decaying quickly with distance). For H^*= 1.83 and ϕ= 0.84, $\mu_{xy} < 0.1$ and θ_s decays linearly with simulation time, indicating very limited translational and rotational particle mobility.

Solid-Mixed-Solid transition

Similar to the case of hexagonal prisms, we map the region of the phase diagram connecting the low density solid (1S) and the high density solid (tetratic phase) over a narrow range of quasi-2D hard confinement separations. As

shown in Fig. 3.11, for H^*= 1.83-1.84 we observe a polycrystalline (mixed P1) phase between the 1S solid and the tetratic-II mesophase, and for $H^* > 1.84$ we detect a similar polycrystalline phase (mixed-P2) connecting directly the tetratic-I and tetratic-II phases as the 1S square solid disappears. Stable 1S solid phase is formed at the lower concentrations since the particles *unflip* to gain z-translational entropy indicated by the widening of the particle distribution function compared to tetratic-II, polycrystalline (P1) and tetratic solid phases (Fig. 3.14).

Figure 3.12 shows the H^*= 1.83 equation of state along with the phase boundaries identified by perusing various orientational and translational order parameters. On compressing the 1S solid phase (which is stable for $\phi < 0.48$) to $0.48 < \phi < 0.78$ (see Fig. 3.12), more particles tend to occupy the *flipped* orientational state as captured by the decrease in the P_{41} and increase in the P_{42} and P_{43} (with similar trends for the corresponding F1, F2, and F3 values). A sharp rise in $S2$ from 0.2 to 0.95 throughout the polycrystalline region (P1) ($0.48 < \phi < 0.78$) provides evidence for the increase in the concentration of *flipped* particles upon compression. Since the four-fold in-plane bond orientational order is broken by the *flipping* of the particles, we observed a decrease in the global value of ψ_4 from 0.9 to 0.43. At ϕ = 0.63, the values of P_{41}, P_{42}, and P_{43} are equal (= 0.54) as are the fractions F1, F2, and F3 (= 0.33). At ϕ = 0.63, this P1 phase (Fig. A.4) exhibits short ranged translational order as captured by the absence of peaks in $g(r)$ beyond the first two neighbor shells and by the low value (0.38) that $g_4(r)$ approaches at long distances. Figure 3.13 further confirms that P1 has short range translational order (as per the diffuse four-fold peaks in (S($\mathbf{k}$)) but a four-fold in-plane orientation of the particle axes. The P1 structures present clusters of the parent 1S solid phase with in-plane orientations along with the tetratic-like

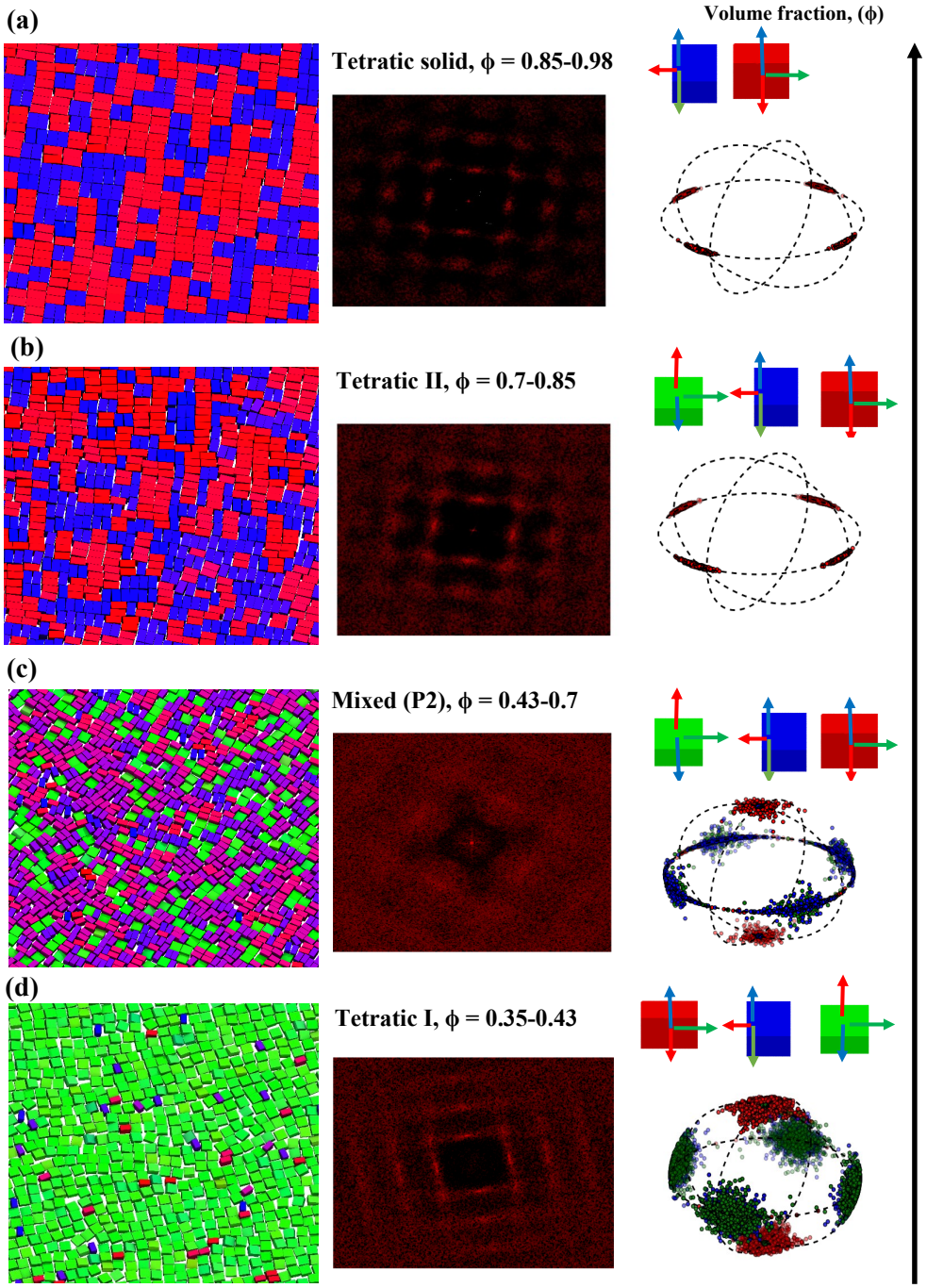

Figure 3.15: Equilibrium structures of square prisms at different concentrations when the hard plate separation is H^*= 1.85. Representative snapshots, structure factors, and particle orientational distribution functions of stable phases (a)-(d) with increasing volume fraction arranged from bottom to top.

clusters formed by the *flipped* particles with no positional order but moderate four-fold bond-orientational order and distinct four-fold in-plane particle axes orientation order. The disappearance of long-range positional order in the P1 region is hence due to the difference in lattice spacing between the (*unflipped*) and *flipped* particle clusters. Further compression to $0.63 < \phi < 0.78$ leads to an increase in the population of *flipped* particles, giving rise to the tetratic-II phase with quasi-(long) range four-fold bond orientational order. The cubatic orientation order parameters P_{41} (F1), and P_{42} (F2) increase and P_{43} (F3) decreases upon compression due to the increase of biaxial ordering of the *flipped* particles and the decrease in the fraction of the *unflipped* particles. Importantly, the P1 phase has very low μ_{xy} values (Fig. 3.12) indicative of the low particle mobility associated with the marginal local free volume available.

The phase behavior for H^*= 1.85 is similar to that for H^*= 1.83, but now a mixed (P2) phase is predicted upon compression of the tetratic-I phase (stable for $\phi < 0.43$). This P2 phase is found for $0.43 < \phi < 0.7$, and only differs from the P1 phase is that it has more rotational and translational freedom as shown in Fig. 3.16. Figure 3.15 (c) shows a snapshot, structure factor, and the particle axes distribution for the P2 phase, while Fig. A.5 shows the correlation functions ($g_4(r)$ and $g(r)$) for all the phases found for H^*= 1.85.

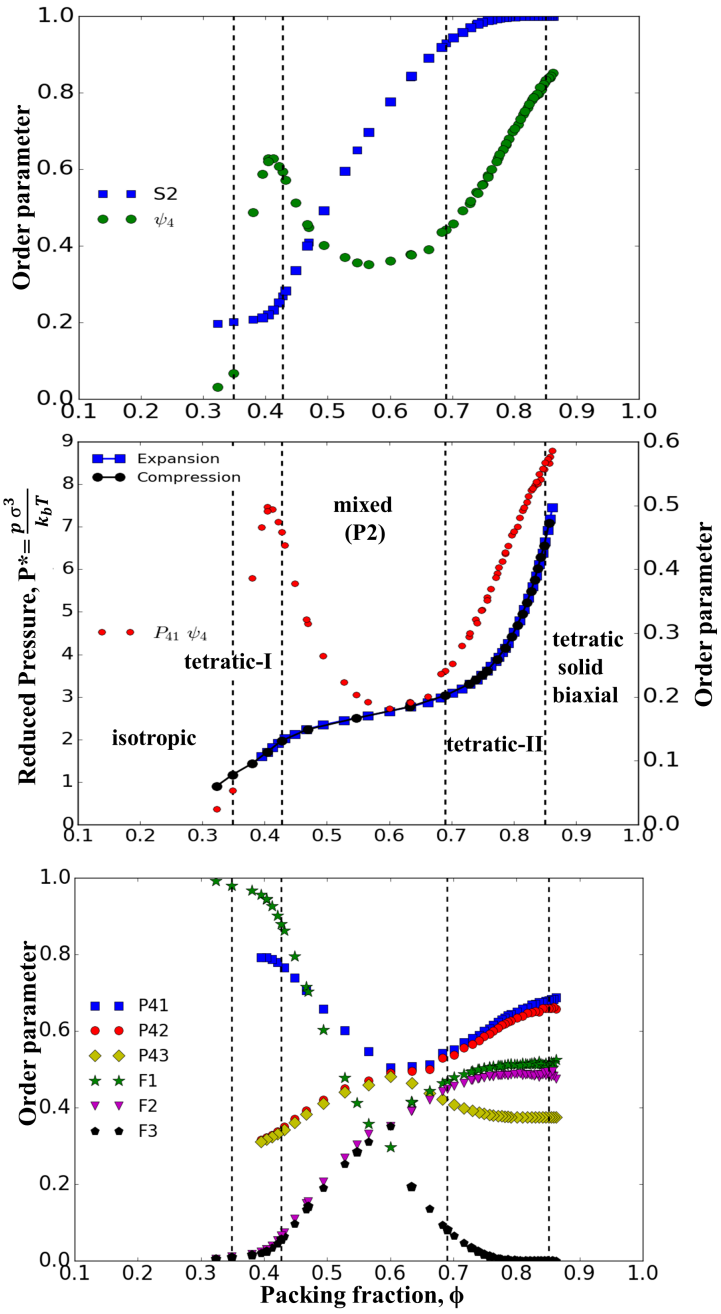

Figure 3.16: Phase behavior of square prisms under hard plate separation, H^*= 1.85. Dotted lines mark the approximate phase boundaries. (Top) Variation of $S2$, ψ_4 and ψ_6 order parameters with packing fraction, ϕ. (Middle) Equation of state (P^* *vs.* ϕ) showing compression and expansion runs and cross order parameters $P_{41}\psi_4$ and $P_{41}\psi_6$. (Bottom) Variation with ϕ of orientational order parameters (P_{41}, P_{42}, P_{43}) and fraction of particles (F1, F2, F3) aligned along the orthogonal directors.

3.2 Bridging rotational states using soft wall confinement model

The solid-solid and solid-dense liquid-solid phase transitions observed for the hexagonal prisms in hard confinement are associated with the broken rotational phase space accessible to the particles, resulting in a forbidden region between the unflipped and flipped states (Fig. 3.17). In particular, the dense liquid phase and tetratic mesophase can be seen as mixed states of flipped and unflipped particles that is only accessible by MC moves able to bridge the broken ergodicity. As one approach to dynamically bridge the gap between these two rotational states and transform forbidden states into merely low-probability states, we implement here a soft confinement model by using a soft repulsive layer coating the bottom wall. In this model, we choose the aspect ratio for hexagonal and square prism particles as 1.82 and 1.67, respectively and fix the separation between the hard walls at 1.95 to allow for dynamic flipping of the particles. The phase transitions observed in hard confinement model are realized by suitable choices of the soft-layer thickness, a^* (Fig. 2.1), and its modulus parameter, β.

Figure 3.18 (a) shows the different types of phase transition sequences, from TYPE 1 to TYPE 4, predicted for the hexagonal prisms under hard confinement. These types of phase transition sequences are mapped for the soft-wall confinement model shown in Fig. 3.18 (b), as obtained for different values of the soft-layer parameters β and a^*. For $a^* = 0.72$, the TYPE 1 phase transition sequence (tetratic solid $\rightarrow$ tetratic mesophase $\rightarrow$ dense liquid (P2) phase) shown in Fig. 3.18 (a), is obtained for $\beta < 6.7$. By decreasing a^*, the β required to attain the TYPE 1 phase sequence expectedly increases, with the boundary between TYPE

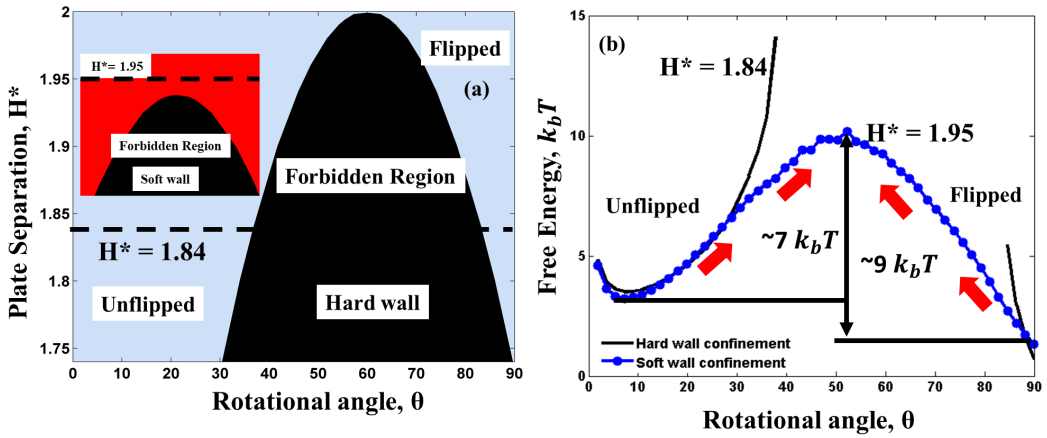

Figure 3.17: (a) Broken ergodic rotational phase map for hexagonal prism in hard confinement and (inset) soft confinement model. Forbidden region bounds the inaccessible rotational states. (b) Rotational free energy for different rotational states for hard walls with H*= 1.84 and for soft wall confinement with H^*= 1.95 for β = 17 and a*= 0.45.

1 and TYPE 2 transition regions being $\beta \approx 8$ for a*= 0.61 and $\beta \approx 14.6$ and a*= 0.45, respectively. For any value of a*, increasing β pushes the phase behavior into TYPE 2 (tetratic solid → tetratic mesophase → dense liquid (P2) → 1Δ) and TYPE 3 phase sequences. The TYPE 3 sequence (Fig. 3.18 (a)) contains two kinds of solid-solid phase transition sequences: tetratic solid → tetratic mesophase → 1Δ and tetratic solid → 1Δ. Further increasing β leads to the TYPE 4 phase sequence, 1Δ → hexatic mesophase, having 2D phase behavior since then the soft-layer is rather "hard" and the effective wall separation corresponds to the hard confinement model having 2D phase behavior.

For β = 17 and a* = 0.45, we used the simulated probability density of different rotational angles to compute the rotational free energy for the particles in the dense liquid phase and estimate the transition barrier from *unflipped* to *flipped*

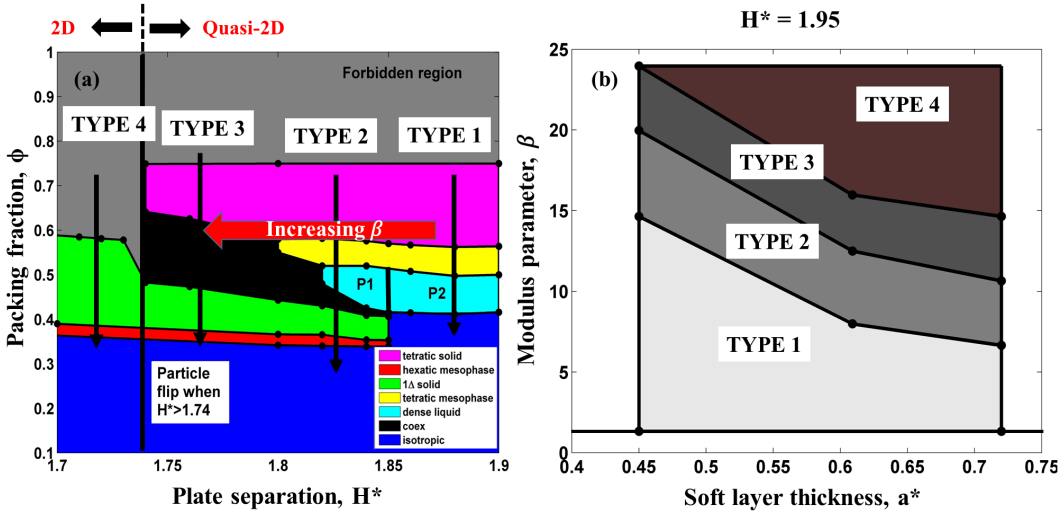

Figure 3.18: (a) Phase diagram of hexagonal prisms under hard-wall confinement marking the different types of phase transition sequences, from TYPE 1 to TYPE 4 (see text for definitions). (b) The different types of phase transition sequences observed using the soft wall model for varying modulus parameter, β, and soft layer thickness, a^*.

states as 7 k_b T and that from *flipped* to *unflipped* states as 9 k_b T (Fig. 3.17b). These barrier values indicate that such *unflipped* $\leftrightarrow$ *flipped* transitions are accessible experimentally but rare events that will require relatively long times to attain thermal equilibration. In principle, the properties of the soft layer could be optimized to speed up the transitions of a particular phase sequence type. We also mapped the phase transition region for the square prisms where the observed correlated effect of β and a^* on phase sequence is similar to that in the hexagonal prisms, as shown in Fig. 3.19. The TYPE 1 (tetratic solid $\rightarrow$ tetratic II mesophase $\rightarrow$ mixed (P2)), TYPE 2 (tetratic solid $\rightarrow$ tetratic II mesophase $\rightarrow$ mixed (P2)$\rightarrow$ tetratic I mesophase), and TYPE 3 (tetratic solid $\rightarrow$ tetratic II mesophase $\rightarrow$ polycrystalline (P1) $\rightarrow$ tetratic I mesophase) phase transition sequences can be attained by increasing β from 1 to 30 for $0.47 < a^* < 0.75$. For

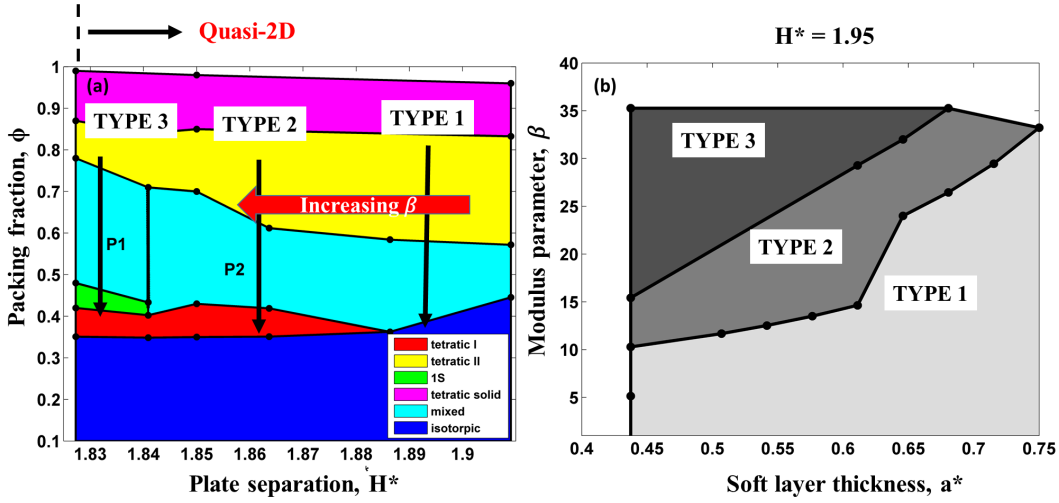

Figure 3.19: (a) Phase diagram for square prisms under quasi-2D hard confinement ($H^* > 1.83$) marking the different types of phase transitions sequences, TYPE 1 to TYPE 3 (see text for definitions). (b) The different types of phase transition sequences observed using the soft wall model for varying modulus parameter, β, and soft layer thickness, a^*.

simplicity, we do not probe the conditions for β and a^*, where the 'trivial' 2D phase bahavior (isotropic → tetratic I mesophase → 1S) sequence occurs.

CHAPTER 4

CONCLUSION

Using Monte Carlo simulations, we first explored the 2D and quasi-2D phase behavior of hard hexagonal and square prisms under hard-slit confinement, by controlling the wall spacing, H^* (with H^*=1 corresponding to the height of the prisms). The 2D phase behaviors observed for hexagonal prisms (for $H^* < 1.74$) and square prisms (for $H^* < 1.83$) are consistent with the known behaviors of hard hexagons and squares, respectively. We focused on larger H^* values where quasi-2D behavior ensues, defined by the range of slit separations which can only fit a monolayer but where particles can be flipped on their sides. We found some similarity in the densest phases formed by hexagonal and square prisms as we predict two types of high-density phases: 1) A tetratic solid having long range four-fold symmetry and translational order, and 2) a tetratic mesophase having quasi-long ranged four-fold order and no translational order. This behavior common to hexagonal and square prisms is due to their having the same in-plane rectangular projected geometry when the particles are flipped. These two shapes exhibit different phase behavior at intermediate and lower concentrations, where the available free volume allows the particles to access the unflipped orientation which changes the projected geometry and area of the shape. Hexagonal prisms with $1.74 < H^* < 1.8$ undergo a first-order phase transition from the tetratic solid phase to the 1Δ (hexagonal close packed) solid. The mechanism for this phase transition is attributed to change from four-fold and six-fold bond lattice symmetry. For $1.82 < H^* < 1.86$, hexagonal prisms were found to form a dense liquid phase between the tetratic mesophase and 1Δ solid indicating a two-stage lattice symmetry breaking mechanism. This dense liquid phase has high particle mobility with no long ranged orientational or transla-

tional order. Square prisms for $1.83 < H^* < 1.84$ exhibit a solid-polycrystalline-solid transition, where the polycrystalline phase has low mobility and weak four-fold bond ordering. This polycrystalline phase then transitions into a 1S solid having four-fold symmetry at lower concentrations through a rearrangement of the lattice spacing.

We proposed a soft repulsive confinement model as a means to overcome the broken dynamic ergodicity that was inherent in the hard confinement model for the range of H^* values studied. A simple soft repulsive model was adopted to represent a soft layer that coats the bottom slit wall. We observed that by varying the modulus parameter, β, and soft-layer thickness, a^*, we can obtain all the distinct phase transition regions mapped for hexagonal prisms and square prisms under hard confinement. Specifically, for a range of a^* where the distance between the top soft layer and bottom hard wall lies in the 2D region of the hard slit phase diagram, we can obtain all the phase transition sequences observed in the quasi-2D region by gradually hardening a sufficienly thick soft layer (increasing β). For the dense liquid phase obtained at $\beta = 17$ and $a^* = 0.45$, we estimate the transition barrier from the unflipped to flipped state to be about 9 k_bT, a rather large value indicates that, while experimentally viable, such transitions are rare events that would require relatively long times to occur.

Although our proposed soft repulsive model suitably captures the relationship between mechanical properties of the soft coating layer like thickness and modulus and the observed phase behavior, several modifications can be introduced to the soft repulsive potential model based on realistic choices of the soft layer material. For example, a neutral polymer brush potential accounting for the elastic energy and the excluded volume interaction between chains,

would provide a more realistic description of the barrier for particle rotations. A crosslinked gel could be another alternative material for the soft layer where the surface potential would be influenced by the interfacial tension and the contact volume between the gel and the particle.

While our proposed soft confinement model estimated a high *flipped*↔*unflipped* rotation transition barrier, it would also be important to estimate transition timescales which will also depend on the absolute size of the particles and properties of the fluid medium. Note also that gravitational effects could also be important depending on particle size and any density mismatch between particle and fluid [61]. Such kinetic data will allow to more clearly define the practical feasibility of the proposed approach. Transition rate calculations can be carried out using a rare-event sampling simulation techniques like Transition path sampling [62] and forward flux sampling [63, 64].

The unique phase behavior observed for hexagonal prisms stems from the duality in the particle projected geometries when the orientation is flipped and unflipped. Indeed, similar phase behavior can also be extended to other simple shapes like cylinders that can be designed to possess such inherent properties. Particle fabrication with precise control over shape and size monodispersity can be achieved, e.g., via photolithographic approaches [65, 66].

Future work will be focused on providing experimental evidence of the dense liquid phase predicted by using microfabricated prisms confined in a wedge cell. Note also that other approaches can be explored that would provide soft confinement. For example, instead of starting with a slit made of hard walls, one could replace one or both walls by a liquid-liquid interface. In such a case, the particles would be soft-repelled by the (non-solvent) liquid that lies

across any such interface. Such systems could be studied using solvent-explicit coarse-grained models [67] to first accurately model the effect of the nanoprism wetting with the different the liquid molecules and then demonstrate whether such systems could reproduce some key features of the phase behavior found in our soft-confinement model.

APPENDIX A

SUPPLEMENTARY INFORMATION ON CORRELATION FUNCTIONS

A.1 Bond order correlation and radial distribution function analysis

A.1.1 Hexagonal prisms

H*= 1.8

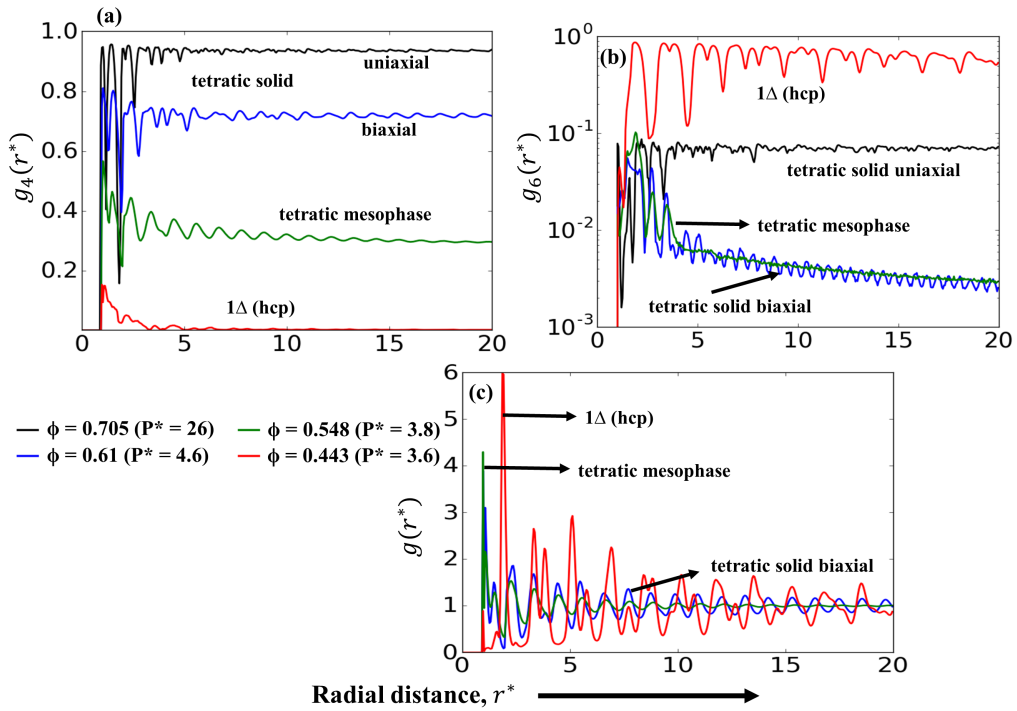

Figure A.1: Correlation functions for hexagonal prisms under a hard confinement separation, H^*= 1.8. (a)-(b) Bond order correlation functions, g_4 and g_6 (c) radial $g(r)$ distribution function for the tetratic solid uniaxial and biaxial, tetratic mesophase, and 1Δ solid. r^* is the scaled radial distance.

H*= 1.84

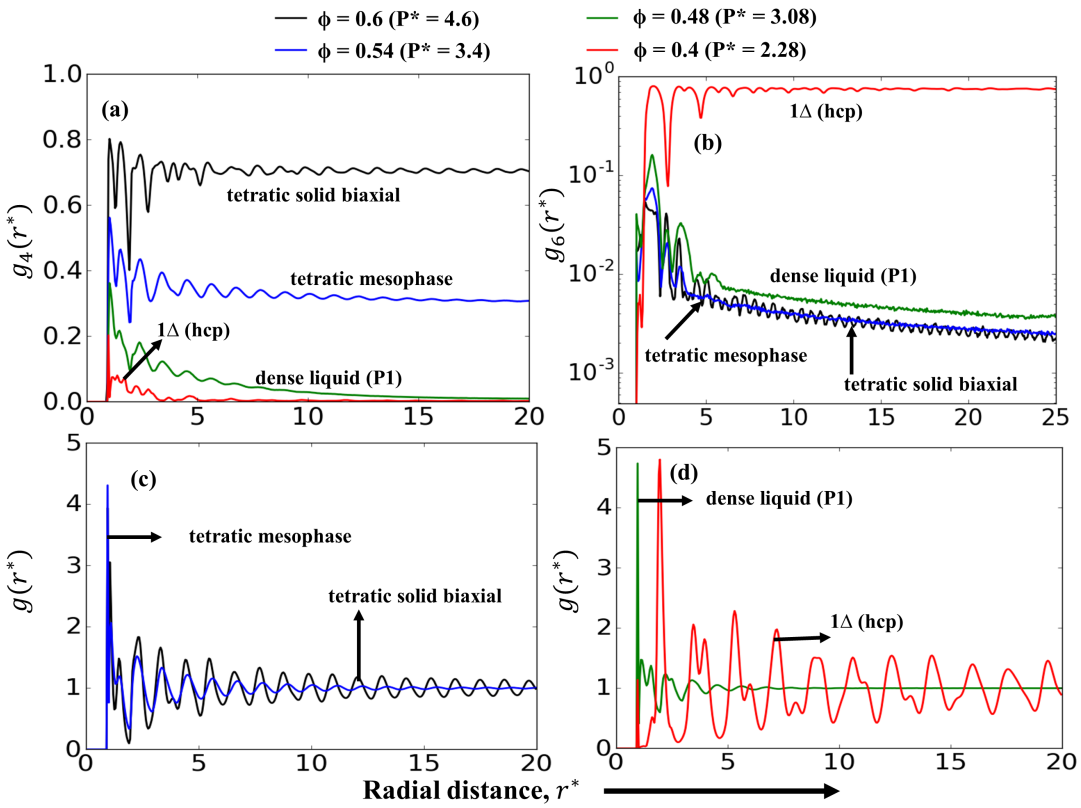

Figure A.2: Correlation functions for hexagonal prisms under hard plate separation H^*= 1.84. (a)-(b) Bond order correlation functions, g_4 and g_6, and (c)-(d) radial $g(r^*)$ distribution function for the tetratic solid biaxial, tetratic mesophase, dense liquid (P1), and 1Δ (hexagonal close packed) solid phases. r^* is the scaled radial distance.

H*= 1.9

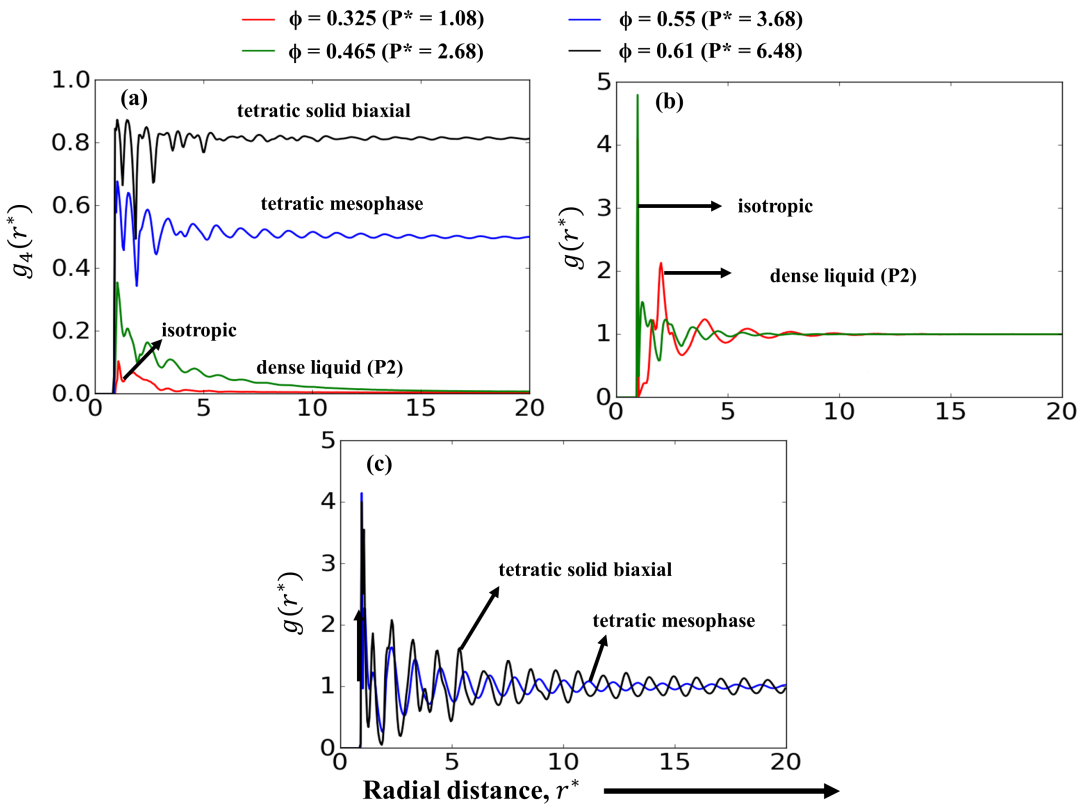

Figure A.3: Correlation functions for hexagonal prisms under hard plate separation H^*= 1.9. (a) Bond order correlation function, g_4, and (b)-(c) radial $g(r^*)$ distribution for the tetratic solid biaxial, tetratic mesophase, dense liquid (P2), and isotropic phases. r^* is the scaled radial distance.

A.1.2 Square prisms

H*= 1.83

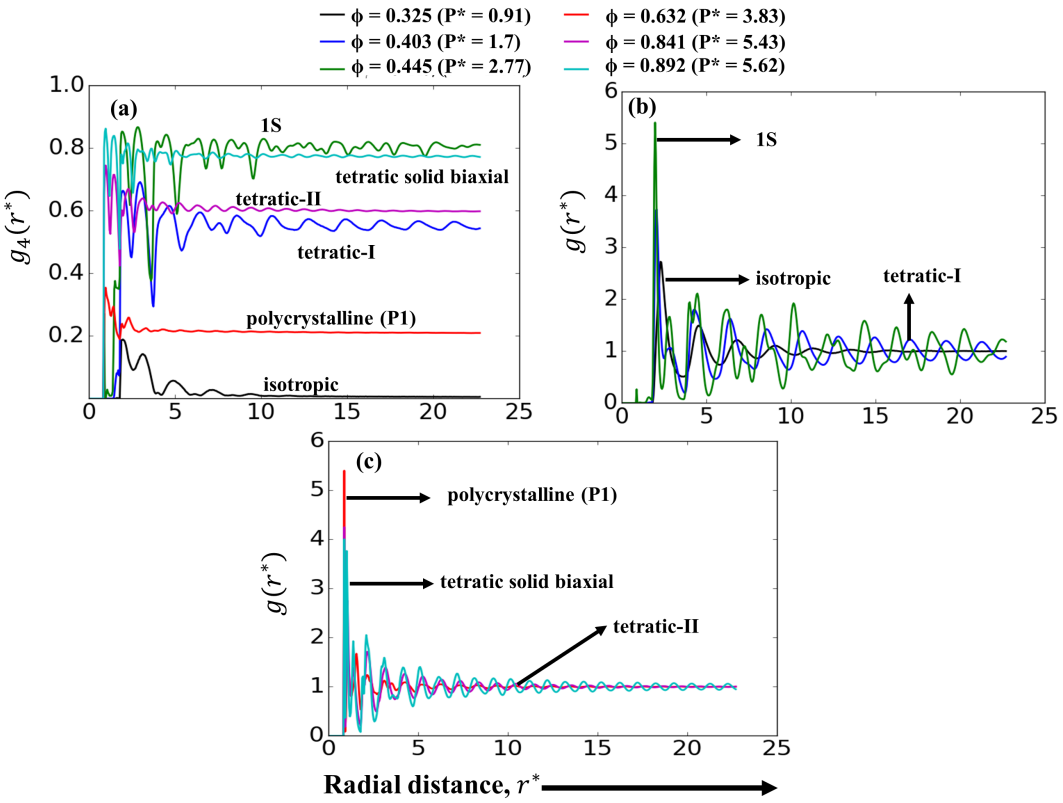

Figure A.4: Correlation functions for square prisms under a hard confinement separation, H^*= 1.83. (a) Bond order correlation functions, g_4 for tetratic solid biaxial, tetratic-II, polycrystalline (P1), 1S, tetratic-I and isotropic phases. Radial $g(r^*)$ for (b) isotropic, tetratic-I, 1S, and (c) tetratic-II, tetratic solid biaxial, and polycrystalline (P1) phases. r^* is the scaled radial distance.

H*= 1.85

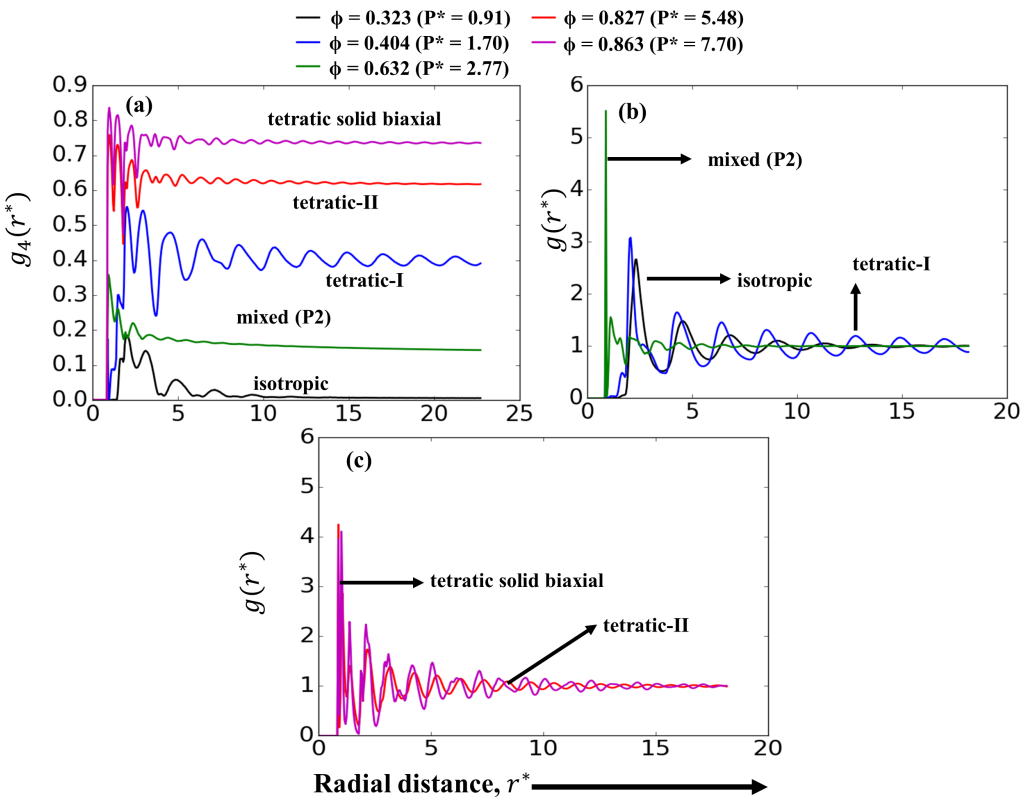

Figure A.5: Correlation functions for square prisms under a hard confinement separation, H^*= 1.85. (a) Bond order correlation functions, $g_4(r^*)$ for tetratic solid biaxial, tetratic-II, mixed (P2), tetratic-I and isotropic phases. Radial distribution function, $g(r^*)$ for (b) isotropic, tetratic-I, mixed (P2), and (c) tetratic-II, tetratic solid biaxial phases.

A.2 Translational and rotational mobility analysis

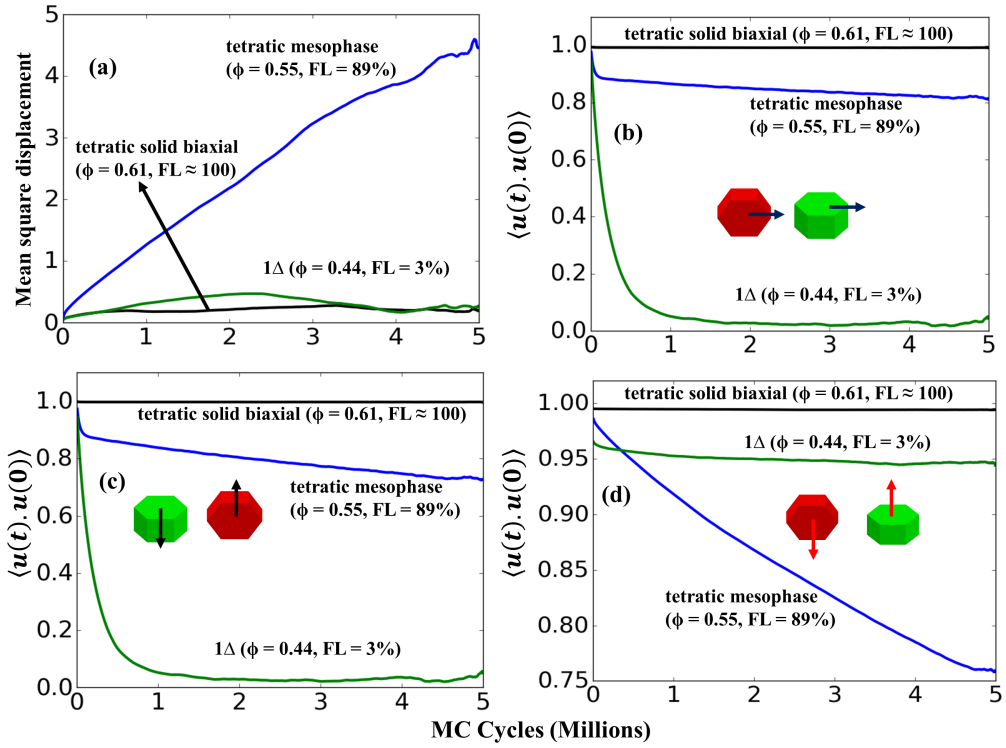

Figure A.6: Mean square displacement (a) and rotational autocorrelation function for all three particle axes (b), (c), (d), against Monte Carlo cycles for tetratic solid biaxial, tetratic, and 1Δ phase at a hard plate separation, H^*= 1.8. The fraction of *flipped* particles (FL) is specified at different packing fractions.

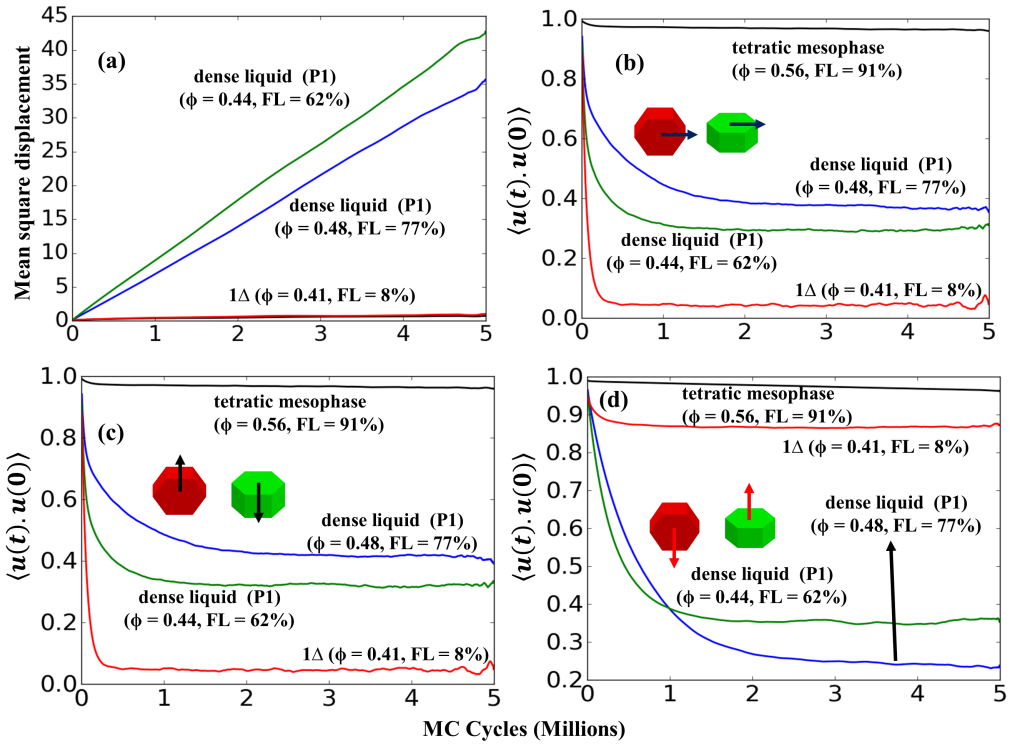

Figure A.7: Mean square displacement (a) and rotational autocorrelation function for all three particle axes (b), (c), (d) against Monte Carlo cycles for tetratic solid, tetratic, P1 and 1Δ phase at a hard plate separation, H^*= 1.84. The fraction of *flipped* particles (FL) is specified at different packing fractions.

APPENDIX B

SUPPLEMENTARY INFORMATION ON 2D PHASE BEHAVIOR

B.1 Hexagonal prisms

The phase behavior at strong hard confinement is similar to that of hard hexagons in a 2D plane, where the upon increasing volume fraction the system transitions from the disordered fluid to a 1Δ hexagonal order solid with an intermediate hexatic-like order mesophase. At low concentrations, the system has low values of the four-fold (ψ_4) and six-fold (ψ_6) bond orientational order parameters, indicative of a disordered phase. Figure B.1 (a) shows the equation of state for H^*= 1.1. As P^* is increased (> 2.0) and $0.597 < \phi < 0.621$, the particles assemble into a partially ordered structure with the characteristics of the hexatic phase (Fig. B.1 (a)) having global $\psi_6 = 0.4 - 0.5$ and $\psi_4 \approx 0$. The system then assembles into a more ordered solid structure as P^* is further increased forming the 1Δ solid that has both long-range translational and orientational order with $\psi_6 = 0.7 - 1.0$. Similar phase behavior has also been observed for hard hexagons (2D model) as described by [51], where the fluid-hexatic and hexatic-solid phase transitions are continuous.

The nature of the translational and bond-orientational order is further characterized by examining the $g_6(r)$ and $g(r)$ functions in Fig. B.1 (b) and (c) at four different conditions close to the isotropic-hexatic-solid transition region. It can be observed that the isotropic phase, with no translational and bond-orientational order (short-range $g_6(r)$ function), transitions into the partially ordered hexatic phase with short-range translational order (decaying $g(r)$ peaks) and quasi-long ranged six-fold bond orientational order, where the correlation

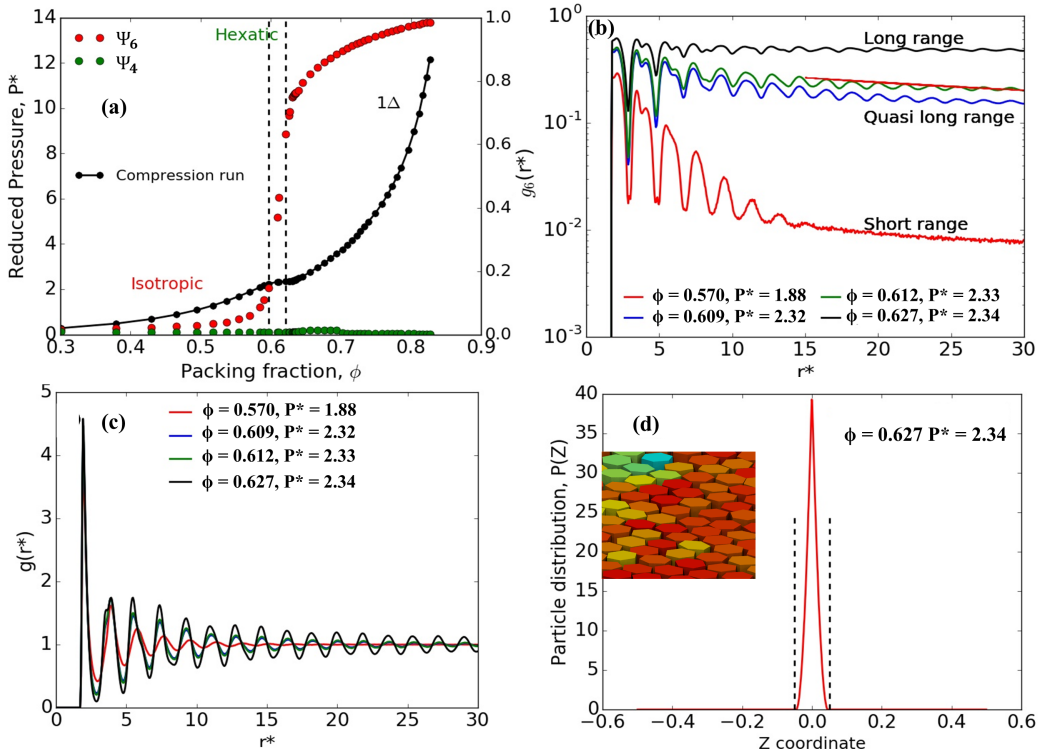

Figure B.1: Equation of state and correlation functions for N= 1254 hexagonal prisms obtained by compression runs for H^*= 1.1. (a) Variation of P^*, ψ_6, and ψ_4 as a function of packing fraction, ϕ. Bond-order correlation function, $g_6(r)$ (b), and radial distribution function, $g(r)$ (c) corresponding to the Isotropic, Hexatic, and Solid phases. The red dashed-line (b) with slope 0.14 corresponds to the algebraic decaying of the correlations in the hexatic-solid transition. (d) Z-coordinate particle distribution function for the solid phase at P^*= 2.344.

function, $g_6(r)$ decays algebraically as $g_6(r) \approx r^{-\eta}$, with η= 0.14 for P^*= 2.328 and ϕ= 0.612.

The plot of $S(\mathbf{k})$ in Fig. B.2 shows short-ranged positional order (diffusive peaks) for the hexatic mesophase and long-ranged order (distinct peaks) the 1Δ solid. At high density and H^*= 1.1, the Z-coordinate distribution (Fig. B.1) is quite narrow, reflecting a small leeway in the z-direction. Figure B.3 shows that as H^* is increased ($1.2 < H^* < 1.74$), the distributions become broader, reflecting

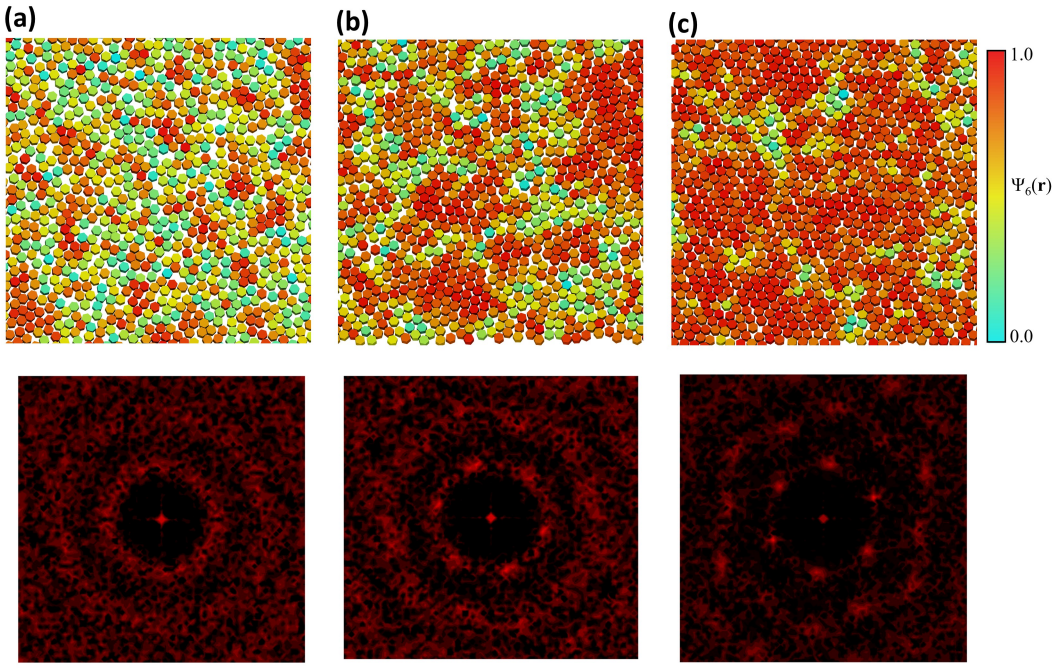

Figure B.2: (Top panel) Snapshots for (a) isotropic (P^*= 1.88, ϕ= 0.57), (b) Hexatic (P^*= 2.328, ϕ= 0.612), and (c) (1Δ) Solid phase (P^*= 2.344, ϕ= 0.627) for a system of N= 1254 hexagonal prisms, including the corresponding structure factor, $S(\mathbf{k})$ (bottom panel). Particles are colored based on the local ψ_6 values shown in the color bar.

the fact that the system increases configurational entropy by exploring positions available in the z-direction. These larger fluctuation along the z-axis occur even at high concentrations and lead to more particle misalignment within the monolayer.

All the distributions in Fig B.3 are unimodal and the large fluctuations indicate that the particles have large local displacement modes similar to vibrational normal modes, which is a key contributor to the free energy of hard-core solids. The 2D-like phase behavior as described in this section is observed for $H^* < 1.74$ and also extends to the quasi-2D confinement separations, H^* up to 1.85 at low

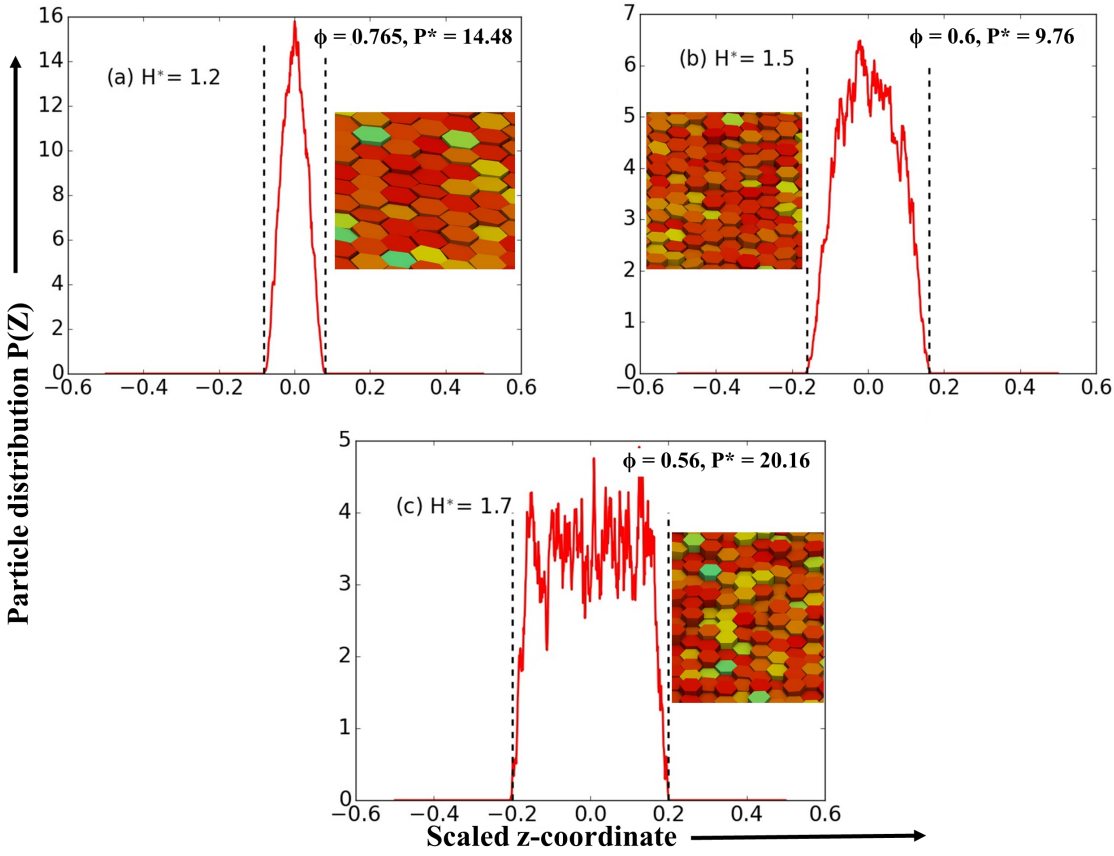

Figure B.3: Z-coordinate particle distribution for the crystal structures at H^*= 1.2(a), 1.5(b), 1.7(c). The dotted lines show the bounds of accessible states. (Insets) Snapshots showing the misalignment of particles along the z-axis.

and intermediate concentrations (0.35< ϕ < 0.48) as shown in Fig. 3.1 (b). Minimum hysteresis in the 2D phase behavior was observed across all transition points between expansion and compression runs, which allowed us to narrow down the location of the phase boundaries.

B.2 Square prisms

We observe 2D phase behavior for 1.83 < H^* < 1.84 and ϕ < 0.48-0.42. The 2D phase behavior for hard squares has been studied by [51] who showed that it follows a KTHNY-type of continuous transition between isotopic and tetratic phase and a continuous transition from the tetratic to solid phase (square lattice-1S). Figure 3.12 shows the 2D phase diagram for ϕ < 0.48 and H^*= 1.83. On compressing the isotropic phase, ψ_4 increases to a moderate value of 0.55-0.6 when forming the tetratic-I phase and then reaches ψ_4= 0.85-0.9 when forming the 1S solid. These transitions are shown in Fig. B.4 for H^*= 1.83. The tetratic-I mesophase exhibits quasi-long range four-fold bond orientational order (g_4) with an average local value of 0.55, and short range translational order, characterized by a fast decay of the $g(r)$ peaks and a diffused four-fold $S(\mathbf{k})$ peaks. The 1S phase has long-range translational order (i.e., slowly-decaying $g(r)$ peaks and distinct four-fold $S(\mathbf{k})$ peaks) and four-fold bond orientational order (in g_4). Figure A.4 shows the trends in $g(r)$ and ψ_4 for H^*= 1.83 for the tetratic-I and the 1S solid phases. For the 0.35 < ϕ < 0.48 region (tetratic-I → 1S), a small increase in P_{41} (0.82-0.86) on compressing is observed due to a stronger in-plane alignment of the square prisms while transitioning from tetratic-I to 1S phase (Fig. 3.12). A similar trend is observed for P_{42} and P_{43}, with values (0.31-0.33) lower than P_{41} since their directors are perpendicular to the particles' principal axis. A sharp increase in $P_{41}\psi_4$ from 0.08 to 0.79 is also observed across the tetratic-I → 1S transition, primarily arising from the significant increase in ψ_4. The low value of $S2$ (≈ 0.17-0.16) and high values of F1 ≈ 1 (and low values of F2 and F3) confirm the prevalence of in-plane particle orientations for these range of ϕ. Since most particles assume in-plane orientation throughout the 2D phase behavior region,

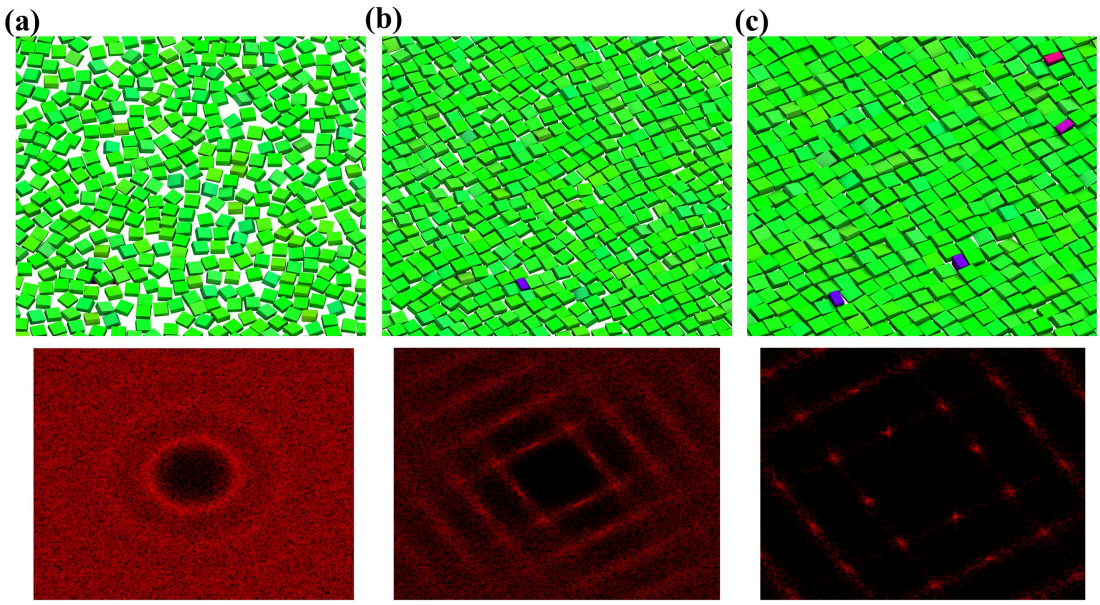

Figure B.4: (Top panel) Snapshots showing the disorder to order transition with (a) isotropic (P^*= 0.9, ϕ= 0.325), (b) Tetratic-I (P^*= 1.7, ϕ= 0.403), and (c) 1S Solid phase (P^*= 2.8, ϕ= 0.445) for a system of N= 1600 along with the corresponding structure factor, $S(\mathbf{k})$ (Bottom panel). *unflipped* and *flipped* particles are colored green and red/blue respectively.

the presence of free volume in the z-direction causes misalignment along the z-axis. Figure 3.14 (a) shows the Z-coordinate distribution at three different conditions corresponding to the isotropic (P^*= 0.9, ϕ= 0.325), tetratic-I mesophase (P^*= 1.7, ϕ= 0.403) and 1S solid (P^*= 2.8, ϕ= 0.445). This distribution gets slightly wider (increasing standard deviation) upon compressing the isotropic phase to tetratic-I mesophase and 1S solid phase but the distribution narrows down near the slit center plane as some particles are *flipped* (as captured by the non zero values of F2 and F3).

BIBLIOGRAPHY

[1] Y.-F. Lim, J. J. Choi, and T. Hanrath, "Facile synthesis of colloidal cuo nanocrystals for light-harvesting applications," *Journal of Nanomaterials*, vol. 2012, p. 4, 2012.

[2] T. Ung, L. M. Liz-Marzan, and P. Mulvaney, "Optical properties of thin films of au@ sio2 particles," *The Journal of Physical Chemistry B*, vol. 105, no. 17, pp. 3441–3452, 2001.

[3] O. D. Velev and S. Gupta, "Materials fabricated by micro-and nanoparticle assembly–the challenging path from science to engineering," *Advanced Materials*, vol. 21, no. 19, pp. 1897–1905, 2009.

[4] B. Liu, T. H. Besseling, M. Hermes, A. F. Demirörs, A. Imhof, and A. Van Blaaderen, "Switching plastic crystals of colloidal rods with electric fields," *Nature communications*, vol. 5, p. 3092, 2014.

[5] U. Agarwal and F. A. Escobedo, "Mesophase behaviour of polyhedral particles," *Nature materials*, vol. 10, no. 3, p. 230, 2011.

[6] S. C. Glotzer and M. J. Solomon, "Anisotropy of building blocks and their assembly into complex structures," *Nature materials*, vol. 6, no. 8, p. 557, 2007.

[7] D. Baranov, A. Fiore, M. van Huis, C. Giannini, A. Falqui, U. Lafont, H. Zandbergen, M. Zanella, R. Cingolani, and L. Manna, "Assembly of colloidal semiconductor nanorods in solution by depletion attraction," *Nano letters*, vol. 10, no. 2, pp. 743–749, 2010.

[8] K. Yaman, C. Jeppesen, and C. Marques, "Depletion forces between two spheres in a rod solution," *EPL (Europhysics Letters)*, vol. 42, no. 2, p. 221, 1998.

[9] T. Biben, P. Bladon, and D. Frenkel, "Depletion effects in binary hard-sphere fluids," *Journal of Physics: Condensed Matter*, vol. 8, no. 50, p. 10799, 1996.

[10] A. Fortini and M. Dijkstra, "Phase behaviour of hard spheres confined between parallel hard plates: manipulation of colloidal crystal structures by confinement," *Journal of Physics: Condensed Matter*, vol. 18, no. 28, p. L371, 2006.

[11] M. R. Khadilkar and F. A. Escobedo, "Phase behavior of polyhedral nanoparticles in parallel plate confinement," *Soft matter*, vol. 12, no. 5, pp. 1506–1516, 2016.

[12] D. Deb, A. Winkler, M. H. Yamani, M. Oettel, P. Virnau, and K. Binder, "Hard sphere fluids at a soft repulsive wall: A comparative study using monte carlo and density functional methods," *The Journal of chemical physics*, vol. 134, no. 21, p. 214706, 2011.

[13] C. Avendano, C. M. L. Watson, and F. A. Escobedo, "Directed self-assembly of spherical caps via confinement," *Soft Matter*, vol. 9, no. 38, pp. 9153–9166, 2013.

[14] K. Muangnapoh, C. Avendaño, F. A. Escobedo, and C. M. L. Watson, "Degenerate crystals from colloidal dimers under confinement," *Soft matter*, vol. 10, no. 48, pp. 9729–9738, 2014.

[15] Y. Min, M. Akbulut, K. Kristiansen, Y. Golan, and J. Israelachvili, "The role of interparticle and external forces in nanoparticle assembly," *Nature materials*, vol. 7, no. 7, p. 527, 2008.

[16] K. Busch and S. John, "Photonic band gap formation in certain self-organizing systems," *Physical Review E*, vol. 58, no. 3, p. 3896, 1998.

[17] C. M. Soukoulis, *Photonic band gap materials*. Springer Science & Business Media, 2012, vol. 315.

[18] E. Yablonovitch, "Photonic band-gap structures," *JOSA B*, vol. 10, no. 2, pp. 283–295, 1993.

[19] K. P. Velikov, A. Moroz, and A. van Blaaderen, "Photonic crystals of core-shell colloidal particles," *Applied Physics Letters*, vol. 80, no. 1, pp. 49–51, 2002.

[20] S.-M. Yang, S.-H. Kim, J.-M. Lim, and G.-R. Yi, "Synthesis and assembly of structured colloidal particles," *Journal of Materials Chemistry*, vol. 18, no. 19, pp. 2177–2190, 2008.

[21] I. D. Hosein and C. M. Liddell, "Convectively assembled nonspherical mushroom cap-based colloidal crystals," *Langmuir*, vol. 23, no. 17, pp. 8810–8814, 2007.

[22] J. T. Overvelde, J. C. Weaver, C. Hoberman, and K. Bertoldi, "Rational design of reconfigurable prismatic architected materials," *Nature*, vol. 541, no. 7637, p. 347, 2017.

[23] N. F. Carnahan and K. E. Starling, "Equation of state for nonattracting rigid spheres," *The Journal of Chemical Physics*, vol. 51, no. 2, pp. 635–636, 1969.

[24] B. de Braaf, M. Oshima Menegon, S. Paquay, and P. van der Schoot, "Self-organisation of semi-flexible rod-like particles," *The Journal of Chemical Physics*, vol. 147, no. 24, p. 244901, 2017.

[25] P. J. Camp and M. P. Allen, "Phase diagram of the hard biaxial ellipsoid fluid," *The Journal of chemical physics*, vol. 106, no. 16, pp. 6681–6688, 1997.

[26] N. Tasios and M. Dijkstra, "A simulation study on the phase behavior of hard rhombic platelets," *The Journal of chemical physics*, vol. 146, no. 14, p. 144901, 2017.

[27] G. Avvisati and M. Dijkstra, "Phase separation and self-assembly in a fluid of mickey mouse particles," *Soft Matter*, vol. 11, no. 43, pp. 8432–8440, 2015.

[28] C. Avendaño and F. A. Escobedo, "Phase behavior of rounded hard-squares," *Soft Matter*, vol. 8, no. 17, pp. 4675–4681, 2012.

[29] P. F. Damasceno, M. Engel, and S. C. Glotzer, "Predictive self-assembly of polyhedra into complex structures," *Science*, vol. 337, no. 6093, pp. 453–457, 2012.

[30] H. Maeda and Y. Maeda, "Liquid crystal formation in suspensions of hard rodlike colloidal particles: direct observation of particle arrangement and self-ordering behavior," *Physical review letters*, vol. 90, no. 1, p. 018303, 2003.

[31] I. D. Hosein, S. H. Lee, and C. M. Liddell, "Dimer-based three-dimensional photonic crystals," *Advanced Functional Materials*, vol. 20, no. 18, pp. 3085–3091, 2010.

[32] C. P. Lapointe, T. G. Mason, and I. I. Smalyukh, "Shape-controlled colloidal interactions in nematic liquid crystals," *Science*, vol. 326, no. 5956, pp. 1083–1086, 2009.

[33] K. Zhao, R. Bruinsma, and T. G. Mason, "Entropic crystal–crystal transi-

tions of brownian squares," *Proceedings of the National Academy of Sciences*, vol. 108, no. 7, pp. 2684–2687, 2011.

[34] E. K. Riley and C. M. Liddell, "Confinement-controlled self assembly of colloids with simultaneous isotropic and anisotropic cross-section," *Langmuir*, vol. 26, no. 14, pp. 11 648–11 656, 2010.

[35] E. G. Teich, G. van Anders, D. Klotsa, J. Dshemuchadse, and S. C. Glotzer, "Clusters of polyhedra in spherical confinement," *Proceedings of the National Academy of Sciences*, vol. 113, no. 6, pp. E669–E678, 2016.

[36] L. B. Cortes, Y. Gao, R. P. Dullens, and D. G. Aarts, "Colloidal liquid crystals in square confinement: isotropic, nematic and smectic phases," *Journal of Physics: Condensed Matter*, vol. 29, no. 6, p. 064003, 2016.

[37] T. Geigenfeind, S. Rosenzweig, M. Schmidt, and D. de las Heras, "Confinement of two-dimensional rods in slit pores and square cavities," *The Journal of Chemical Physics*, vol. 142, no. 17, p. 174701, 2015.

[38] P. Pieranski, L. Strzelecki, and B. Pansu, "Thin colloidal crystals," *Physical Review Letters*, vol. 50, no. 12, p. 900, 1983.

[39] S. Neser, C. Bechinger, P. Leiderer, and T. Palberg, "Finite-size effects on the closest packing of hard spheres," *Physical review letters*, vol. 79, no. 12, p. 2348, 1997.

[40] F. Ramiro-Manzano, E. Bonet, I. Rodriguez, and F. Meseguer, "Layering transitions in colloidal crystal thin films between 1 and 4 monolayers," *Soft Matter*, vol. 5, no. 21, pp. 4279–4282, 2009.

[41] E. C. Oğuz, M. Marechal, F. Ramiro-Manzano, I. Rodriguez, R. Messina, F. J. Meseguer, and H. Löwen, "Packing confined hard spheres denser with adaptive prism phases," *Physical review letters*, vol. 109, no. 21, p. 218301, 2012.

[42] M. Schmidt and H. Löwen, "Freezing between two and three dimensions," *Physical review letters*, vol. 76, no. 24, p. 4552, 1996.

[43] E. C. Oğuz, R. Messina, and H. Löwen, "Crystalline multilayers of the confined yukawa system," *EPL (Europhysics Letters)*, vol. 86, no. 2, p. 28002, 2009.

[44] A. B. Fontecha, H. J. Schöpe, H. König, T. Palberg, R. Messina, and H. Löwen, "A comparative study on the phase behaviour of highly charged colloidal spheres in a confining wedge geometry," *Journal of Physics: Condensed Matter*, vol. 17, no. 31, p. S2779, 2005.

[45] Y. Peng, F. Wang, Z. Wang, A. M. Alsayed, Z. Zhang, A. G. Yodh, and Y. Han, "Two-step nucleation mechanism in solid–solid phase transitions," *Nature materials*, vol. 14, no. 1, p. 101, 2015.

[46] P. Gurin, S. Varga, M. González-Pinto, Y. Martínez-Ratón, and E. Velasco, "Ordering of hard rectangles in strong confinement," *The Journal of Chemical Physics*, vol. 146, no. 13, p. 134503, 2017.

[47] J. Robinson, M. Godfrey, and M. Moore, "Glasslike behavior of a hard-disk fluid confined to a narrow channel," *Physical Review E*, vol. 93, no. 3, p. 032101, 2016.

[48] A. C. Stelson, S. J. Penterman, and C. M. L. Watson, "Hierarchical fullerene assembly: Seeded coprecipitation and electric field directed assembly," *Small*, vol. 13, no. 17, 2017.

[49] D. Wan and S. C. Glotzer, "Shapes within shapes: how particles arrange inside a cavity," *arXiv preprint arXiv:1801.02087*, 2018.

[50] J. M. Kosterlitz and D. J. Thouless, "Ordering, metastability and phase transitions in two-dimensional systems," *Journal of Physics C: Solid State Physics*, vol. 6, no. 7, p. 1181, 1973.

[51] J. A. Anderson, J. Antonaglia, J. A. Millan, M. Engel, and S. C. Glotzer, "Shape and symmetry determine two-dimensional melting transitions of hard regular polygons," *Physical Review X*, vol. 7, no. 2, p. 021001, 2017.

[52] E. G. Gilbert, D. W. Johnson, and S. S. Keerthi, "A fast procedure for computing the distance between complex objects in three-dimensional space," *IEEE Journal on Robotics and Automation*, vol. 4, no. 2, pp. 193–203, 1988.

[53] S. Cameron, "Enhancing gjk: Computing minimum and penetration distances between convex polyhedra," in *Robotics and Automation, 1997. Proceedings., 1997 IEEE International Conference on*, vol. 4. IEEE, 1997, pp. 3112–3117.

[54] H. Ong, H. Huang, and W. Huin, "Finding the exact volume of a polyhedron," *Advances in Engineering Software*, vol. 34, no. 6, pp. 351–356, 2003.

[55] K. Wojciechowski, D. Frenkel, and A. Brańka, "Nonperiodic solid phase in a two-dimensional hard-dimer system," *Physical review letters*, vol. 66, no. 24, p. 3168, 1991.

[56] J. de Graaf, L. Filion, M. Marechal, R. van Roij, and M. Dijkstra, "Crystal-structure prediction via the floppy-box monte carlo algorithm: Method and application to hard (non) convex particles," *The Journal of chemical physics*, vol. 137, no. 21, p. 214101, 2012.

[57] B. S. John, C. Juhlin, and F. A. Escobedo, "Phase behavior of colloidal hard perfect tetragonal parallelepipeds," *The Journal of chemical physics*, vol. 128, no. 4, p. 044909, 2008.

[58] A. Donev, J. Burton, F. H. Stillinger, and S. Torquato, "Tetratic order in the phase behavior of a hard-rectangle system," *Physical Review B*, vol. 73, no. 5, p. 054109, 2006.

[59] K. Zhang, "On the concept of static structure factor," *arXiv preprint arXiv:1606.03610*, 2016.

[60] K. Zhao, C. Harrison, D. Huse, W. Russel, and P. Chaikin, "Nematic and almost-tetratic phases of colloidal rectangles," *Physical Review E*, vol. 76, no. 4, p. 040401, 2007.

[61] J. M. McBride and C. Avendaño, "Phase behaviour and gravity-directed self assembly of hard convex spherical caps," *Soft matter*, vol. 13, no. 10, pp. 2085–2098, 2017.

[62] C. Dellago, P. G. Bolhuis, F. S. Csajka, and D. Chandler, "Transition path sampling and the calculation of rate constants," *The Journal of Chemical Physics*, vol. 108, no. 5, pp. 1964–1977, 1998.

[63] R. J. Allen, D. Frenkel, and P. R. ten Wolde, "Forward flux sampling-type schemes for simulating rare events: Efiiciency analysis," *The Journal of chemical physics*, vol. 124, no. 19, p. 194111, 2006.

[64] R. J. Allen, P. B. Warren, and P. R. Ten Wolde, "Sampling rare switching events in biochemical networks," *Physical review letters*, vol. 94, no. 1, p. 018104, 2005.

[65] S. Badaire, C. Cottin-Bizonne, J. W. Woody, A. Yang, and A. D. Stroock, "Shape selectivity in the assembly of lithographically designed colloidal particles," *Journal of the American Chemical Society*, vol. 129, no. 1, pp. 40–41, 2007.

[66] C. J. Hernandez and T. G. Mason, "Colloidal alphabet soup: Monodisperse dispersions of shape-designed lithoparticles," *The Journal of Physical Chemistry C*, vol. 111, no. 12, pp. 4477–4480, 2007.

[67] U. Gupta, T. Hanrath, and F. Escobedo, "Modeling the orientational and positional behavior of polyhedral nanoparticle at fluid-fluid interfaces," *Physical Review Materials*, vol. 1, no. 5, p. 055602, 2017.